This is to certify that the
dissertation entitled

NEW SIMPLE DSPI SETUPS AND
IMPROVEMENT OF NOISE TOLERANCE OF DSPI

presented by

Xu Ding

has been accepted towards fulfillment
of the requirements for the

_____Ph.D._____ degree in _____Mechanical Engineering_____

_____
Major Professor's Signature

_____13 December 2004_____

Date

PLACE IN RETURN BOX to remove this checkout from your record.
TO AVOID FINES return on or before date due.
MAY BE RECALLED with earlier due date if requested.

DATE DUE	DATE DUE	DATE DUE

6/01 c:/CIRC/DateDue.p65-p.15

NEW SIMPLE DSPI SETUPS AND
IMPROVEMENT OF NOISE TOLERANCE OF DSPI

By

Xu Ding

A DISSERTATION

Submitted to
Michigan State University
in partial fulfillment of the requirements
for the degree of

DOCTOR OF PHILOSOPHY

Department of Mechanical Engineering

2004

ABSTRACT

NEW SIMPLE DSPI SETUPS AND
IMPROVEMENT OF NOISE TOLERANCE OF DSPI

By

Xu Ding

The general objective of this research is to improve the environmental immunity of the digital speckle pattern interferometry (DSPI) technique and simplify the DSPI apparatus so that DSPI can be more robust and cost effective, meaning that this technique can be used for measurement in more realistic industrial environments.

An improved Max-Min scanning method (IMMS) for phase determination has been developed in this research work, and its application to the determination of phase maps was successfully demonstrated in some DSPI. Because signal-processing techniques in the time domain are employed in the new IMMS method, the improved algorithm has shown good environmental tolerance.

By application of the newly developed IMMS method, a new technique to calibrate the phase shifting behavior has been derived. Its applications to check the behavior of piezo electronic transducer (PZT) phase shifters were successfully demonstrated in experiments. This technique uses the IMMS method to compute the phase values along the entire intensity waveform to obtain the diagram of phase shifting versus the driving voltages to the PZT at some pixels, so that the linearity of the phase shifting can be

clearly displayed. By considering more pixel points along chosen directions over the image, the tilt and non-uniformity of the phase shifting can be shown in a 3-D graph. This calibration algorithm eliminates the drawbacks caused by the common assumption of linearity and uniformity of the phase shifter, thus efficiently minimizing the movement error of the PZT. This new calibration method can be used to evaluate a few properties of the phase shifter simultaneously, such as non-linearity, non-uniformity and tilt.

Since the IMMS method shows good environment tolerance, particularly minimizing the effect of errors of phase shifting, both in-plane DSPI and out-of-plane DSPI could be simplified very much compared to the commonly used setups. These simplified setups were shown to work quantitatively with the IMMS phase shifting method. Very good noise immunity of the presented setup was seen. This simplification makes DSPI more cost effective and broadens the application of the electronic speckle pattern interferometry (ESPI) technique to noisy service environments outside the laboratory.

To my parents

ACKNOWLEDGMENTS

TABLE OF CONTENTS

LIST OF TABLES

LIST OF FIGURES

Chapter 1. Introduction

1.1 Problem outline

Speckle pattern interferometry (SPI) is an accurate, non-contact, full-field technique for displacement field measurement on naturally rough surfaces. The employment of phase shifting techniques enhances the precision and the convenience of the SPI technique for quantitative measurement. With the SPI technique, there is no requirement for surface preparations. In addition, the application of electronic detectors and digital signal processing techniques in computers make SPI a real-time measurement technique. The technique is alternatively termed as digital speckle pattern interferometry (DSPI).

The advantages of the DSPI technique are very attractive for many researchers and industries. Unfortunately, the intrinsic sensitivity of the DSPI technique also makes it vulnerable to environmental disturbances such as vibration, beam source fluctuation, air currents, and thermal convection. In addition, the motion of the piezoelectric transducer commonly used to perform phase shifting in DSPI apparatus is not exact, and the CCD detector is not truly linear either. These effects introduce errors in the calculation of measurement results of the DSPI (Phillion 1997). These are the main reasons why the DSPI technique has not found its way to wide factory applications.

To make the DSPI technique more applicable to practical industrial problems, in the past years, a number of researchers have been working on improving the environmental tolerance of the DSPI technique. These research works can be classified into two broad

categories: (1) improvement of the signal-processing algorithm, and, (2) improvement of hardware arrangements for the setup.

A small amount of vibration can introduce large phase errors and these errors are difficult to eliminate from the phase data; but they can be minimized with proper algorithm design. Many of the past works focused on improving signal processing algorithms, including developing new phase evaluation methods, performing new phase unwrapping algorithms, and developing new filtering techniques.

In some situations, where the amount of vibrations is so great that the measurement is not possible with standard phase shifting interferometers, another solution is necessary. A range of partial solutions to the noise sensitivity problem has been developed. These include the use of pulsed lasers to freeze the specimen motion, common-path configurations such as shearing interferometers, active phase-stabilization systems, and dynamic speckle interferometers based on high-speed video cameras. (Ruiz, et al. 2001)

However, in measurement systems that result in nonsinusoidal periodic waveforms (either by choice or by imperfections such as phase-shift errors, multiple interference beams, non-linearity in detector), the performance of existing algorithms is often inadequate (Larkin 1992). It is evident from a survey of literature that much of the effort in the development of phase shifting techniques has been spent on addressing errors introduced by the phase shifting itself. Few reports about improvement of the hardware setup can be found.

1.2 Objectives

In order to make the DSPI setup more robust and cost effective, so that this technique can be practically used for measurement in realistic industry environments, the general objective of this work is to improve the environmental immunity of the DSPI technique and simplify the DSPI apparatus.

Development of a new signal-processing algorithm for phase determination that has an improved noise tolerance is the first choice. It is known that the temporal phase shifting technique requires the recording of at least three phase-shifted interferograms, which must be taken sequentially. The sequential recording of inerferograms can lead to disturbances by thermal and mechanical fluctuations during the required recording steps. In addition, fast object deformations cannot be detected (Bothe, Burke, and Helmers, 1997). However, the time-domain phase shifting techniques offer several advantages, including improved noise immunity, insensitivity to spatial variations in the detector response, high-spatial-frequency resolution, and ease of implementation, over spatial-domain methods of interferogram analysis

In the first part of this research, some digital signal-processing techniques are employed to process the time-domain signals of phase shifting interferometers to improve the noise tolerance of the DSPI technique. Based upon the new algorithm, a simple in-plane sensitive DSPI setup and a new phase shifting out-of-plane sensitive DSPI are implemented to measure displacement fields quantitatively.

By application of the new algorithm, a new calibration method for PZT phase shifters is developed in this work. The new calibration technique offers a convenient on-

line method to evaluate several characteristics of the phase shifter simultaneously, including the non-linearity, tilting, and non-uniformity of the phase shifter motion.

1.3 Relevant literature review

Much development has taken place in digital speckle pattern interferometry techniques during the recent past. Some literature reviews that are relevant to the current research work follow:

A. The development of phase extraction techniques.

Phase shifting techniques are commonly used in interferometers for phase determination. The main idea is to induce some known or unknown phase changes artificially in the interference system to obtain more information so as to determine the phase information that is needed. The phase shifting techniques for speckle pattern interferometry include the three-steps, Carré method, four-steps, seven-steps, Fourier-transform, and sinusoidal curve fitting methods.

As summarized by Cloud (1995), the three-step phase-shifting technique, the four-step phase shifting technique, and the Carré technique are some basic/common phase shifting techniques. The three-step and four-step techniques use a known phase shift obtained by calibrating the phase shifter. In 1966, The Carré technique was devised. This technique uses a constant phase shift step; but it is independent of the amount of the phase shift, which means that calibration of the phase shifter can be omitted. It is believed that the Carré technique has a better error immunity than the other two techniques (Cheng and Wyant 1985).

A single phase-step algorithm was reported by Sesselmann, and Goncalves (1998). By combining intensity equations obtained before and after displacement, only two phase-stepped interferograms with a known phase step for each displacement state are enough to retrieve the phase angle induced by the displacement. However, because this method relies on the accuracy of the phase step, it is very susceptible to noise such as vibrations and air currents that result in serious phase step errors.

Surrel (1996) reported a technique to associate a characteristic polynomial with any phase-shifting algorithm based upon an assumption that the fringe pattern has a sine profile and constant phase step. He demonstrated that a 2j+2 phase step was necessary to obtain insensitivity to the jth harmonic content in the presence of a constant phase-shifting miscalibration. Six-step and ten-step algorithms were derived in his paper.

Several seven-step techniques were reported by Zhang (1998), Larkin and Oreb (1992), De Groot (1995), Hibino, Oreb, Farrant, and Larkin (1995). A Fourier description method was used to expand the intensity equation of the speckle pattern interference. Seven phase steps were used to acquire speckle pattern signals to compute the Fourier coefficients. The differences between these seven step techniques are that different step values were used, and different data processing equations were employed. They were all claimed to be insensitive to the second-harmonic component to some degree.

Farrel and Player (1992) developed a variable step algorithm for phase determination. The Lissajous figure technique and ellipse fitting were employed to detect and quantify phase change between frames with accuracy around 4 degrees. Furthermore, two algorithms for N different steps were presented. Numerical simulations showed the algorithms had poor performance under some specific phase step values. In 1994, an

inter-pixel algorithm and a dual-step algorithm based on the same Lissajous figure and ellipse fitting techniques were reported. The authors pointed out that the computational effort required in these algorithms is much greater than for fixed step algorithms.

An algorithm that is immune to tilt phase-shifting error for phase-shifting interferometers was presented by Chen, Guo, and Wei (2000). It is assumed that the tilt errors are linearly distributed throughout each speckle pattern interferogram so that all pixels remained on the same phase plane after tilt occurs. The first-order Taylor series expansion of the phase shifting error equations was used to determine the actual phase shift plane. Numerical simulations showed that this algorithm could compensate for phase-measurement errors caused by both translation and tilt-shift errors, based upon the assumption that all shifted phases are kept on the same phase-shift plane.

A Fourier-transform method for phase determination was presented by Goldberg and Bokor (2001). Based upon the assumption that the phase increment was uniform throughout all the domain points, a Fourier-transform technique was performed to determine the N global phase positions introduced during the phase shifting steps. Then, the phase positions were substituted into the least-square method as input information to compute the phase angles. The Fourier-transform method relies highly on the fact that the phase shifting process does not change the spatially varying components of the optical path difference, which means the spatial carrier frequency must be high enough to adequately separate the first order signal from the zeroth order components in the Fourier domain. If a large portion of the interferometric data is available, this technique can be very robust in the presence of noise.

The Max-Min scanning method was reported by Vikhagen (1990), and applied by Wang, Grant, (1995), and Chen, Gramaglia, and Yeazell, (2000). In the Max-Min method, the basic idea is that a set of recorded intensity signals is sorted to find the maximum and minimum intensity values at each pixel, and the phase angle is calculated from the values by the following equation.

$$\phi = ArcCos\left(\frac{I - \dfrac{I_{Max} + I_{Min}}{2}}{\dfrac{I_{Max} - I_{Min}}{2}} \right)$$

After the above computations, a small constant step phase shift is performed to obtain additional sign images to determine the sign of the calculated phase value both before and after displacement occurrence.

A sinusoid least square fitting method was reported by Macy and Bokor (1983), and by Ransom and Kokal (1986). In the sinusoid fitting method, an assortment of intensity data was recorded during the phase shifting procedure. The intensity wave was assumed to be of sinusoidal waveform. The sinusoidal fitting model, $I(v)=a(v)+b(v)Cos(\varphi(v))$, was used to fit the recorded signals. After solving a series of equations, fitting parameters, $a(v)$, $b(v)$ and $\varphi(v)$ were determined. Okada, Dato, and Tsujiuchi (1991) modified the least-square method. Both phase shift and phase angle were counted as unknowns simultaneously. Two steps of linear least-square calculations were performed, one to obtain the phase distribution and the other one to obtain the phase shift. The steps were repeated until the results converge.

An active phase-shifting method was reported by Yamaguchi, Liu, Kato (1996). A spatial filtering detector was placed in the setup to detect the fringe movements caused by external perturbations. The detected information was fed back to the PZT phase shifter to stabilize and adjust the phase step.

The spatial phase shifting method (SPSM) has been designed to avoid problems such as fluctuation of beam light and non-linearity of phase shifting motion that arise due to the acquisition of different patterns at different time as is the norm in the above techniques. By combining rotational polarizing components or diffraction optical elements, a set of phase-shifted interferograms can be acquired simultaneously.

Koliopoulos (1996) presented a simultaneous phase shift interferometer(SPSI). The setup of the SPSI differs from the traditional method of obtaining phase shifted interferograms, which use PZT mirrors to physically create computer-controlled phase shifts over a short time period. The SPSI creates four phase-shifted interferograms using polarization optics to simultaneously produce four phase-shifted interferograms. Four CCD cameras are placed in the setup to acquire four interferograms simultaneously. These four cameras are co-aligned on a sub-pixel basis so that any point on the object being tested is seen at the equivalent pixel in each of the four cameras. This phase algorithm is relatively restricted. Additional errors appear because the patterns are obtained by different cameras or from different parts of the same camera, which introduce variations of intensity. Moreover, precise alignment of the optical elements with sub pixel accuracy is required. (Dorrio, Fernandez, 1999, Bothe, Burke, and Helmers 1997).

8

Some methods of freezing the fringe map have been reported also, such as using a pulse laser or a high speed camera (Melozzi, Pezzati, and Mazzoni 1995). They are not discussed here.

If there are no means to perform phase shifting, the Fourier transform technique, the convolution algorithm, the sinusoidal fitting method, and the spatial synchronous detection methods can be some alternatives to evaluate the phase information. It is often believed that the phase shifting methods are more precise than these methods that rely on a single pattern image. These techniques will not be discussed in detail. Corresponding references can be found in Massing and Heppner (2001).

B. Calibration techniques.

The accuracy of most phase shifting techniques relies on the accuracy of the phase step. Even those methods claiming to be insensitive to miscalibration of the phase shifter will benefit from knowing precisely the behavior of the phase shifter. So, the accurate calibration of the phase shifter is still highly desired in many interferometry techniques.

Few methods have been reported for the calibration of phase shifters used in interferometry techniques.

The simplest one is the phase-lock method as mentioned by Cheng and Wyant (1985). Once the two images of fringes, before and after phase stepping, are observed to be identical and all fringes are shifted to the position of their neighbor fringes, the 2π-phase step is determined. This phase-lock method has the advantage that it is not sensitive to nonlinearity of the phase shifter. However, this phase-lock method can only

be used to calibrate the 2π-phase step. Once the 2π phase step has been determined, the intermediate phase steps can be computed by a simple interpolation. The accuracy of the interpolation results strictly depends on the linearity of the phase step schemes.

The Carré phase shifting method was used by Cheng and Wyant (1985) to calibrate the phase shifter. Four phase-shifted interferograms are used in the Carré phase shifting algorithm to determine the phase step. The Carré algorithm can also be used to obtain information on all four unknowns in the intensity equation of speckle interference. This calibration method relies on the assumption of good linear movement of the phase shifter.

A two-image method was reported by Brug (1999). Two intensity images were obtained by a phase step. The correlations between these two phase-stepped intensity images were computed, and then the phase step was retrieved from the correlation result. With this method, the phase changes must be ensured to be linear in the area where the method is applied.

All these methods have some obvious drawbacks and limitations. In addition, none of them can check the detailed behavior of the shifter, i.e., the linearity, the tilt, and the non-uniformity of the phase shifter. A convenient real-time calibration method is desired to thoroughly characterize phase shifters.

C. Simple ESPI setups.

Relatively little research have been published about simplifying the system of apparatus of DSPI. A compact DSPI sensor was introduced by Siebert, Wegner and Ettemeyer (2001), but the construction of that DSPI sensor is still a trade secret.

Several variants of a simple out-of-plane sensitive DSPI setup were reported and patented by Cloud (2000, 2003). To make these simple setups work quantitatively, a method to perform phase shifting is desired. The newly Improved Max-Min Scanning (IMMS) phase shifting algorithm has a good immunity to tilt, non-linearity and non-uniformity of phase shifting as well as vibration noise, as reported by Ding (2002) and by Ding and Cloud (2004). This approach is applicable to other types of phase-shifting interferometry, but it is used here to greatly expand the capability of DSPI.

Chapter 2. Summary of speckle technique

2.1 Introduction

This chapter briefly introduces the digital speckle pattern interferometry technique (DSPI), including the basic theory of speckle interferometry, phase shifting techniques, image processing techniques, and typical DSPI setups. The main sources of the information are Cloud (1995), Hong (1997), and Lanza di Scalea (1996).

2.2 Concept of laser speckles

Illumination of a rough surface (roughness of the order of the wavelength of the illumination light) by a coherent light creates a grainy intensity distribution in space termed a speckle pattern as shown in Figure 2.1. For some years, it was considered a special kind of noise, and it limited the usefulness of lasers. However, with understanding that the speckle is a result of the coherent addition of waves scattered from a rough surface, its information-carrying property was discovered. This discovery led to a new class of optical measurement techniques known as speckle methods.

Laser speckle is categorized into two types: objective speckle and subjective speckle. When an optically rough surface whose roughness is of the order of the wavelength of laser beam is illuminated by laser light, the intensity of the scattered light varies randomly with position. This effect is known as objective speckle. When a lens is used to form an image of the illuminated rough surface, the image shows a similar random intensity variation that is referred to as subjective speckle. The size of the

12

speckles is dependent on the aperture, focal length of the lens, and the wavelength of the illuminating light. The speckle size on the object can be written as:

$$S_{subject} = \frac{1.22 \times (1 + M)\lambda F}{M}$$ (2.1)

Where $S_{subject}$ is the size of the subjective speckles at the object plane;

                                       M is the magnification of the lens;

                                       λ is the wave length of the illumination beam;

                                       F is the aperture ratio (focal length/aperture).

The real speckle size is usually in the range of 5 to 50 μm.

The speckle size at the image is computed by

$$S_{subject} = 1.22 \times (1 + M)\lambda F$$ (2.2)
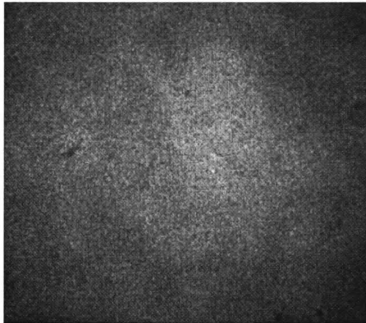
Figure 2.1. Laser speckle.

From this equation, it is known that the resolution of the detector must be greater than the speckle size to fully track the behavior of the speckle. The maximum resolution required of the setup is determined by equation 2.2.

2.3 Speckle pattern interferometry

When a laser speckle pattern is mixed with a second coherent beam, the intensity image of the interference, which has a random speckle appearance, is known as speckle interference. In the following parts, an in-plane sensitive interferometer, as shown in Figure 2.2, will be used to explain the fringe formation of speckle interference.
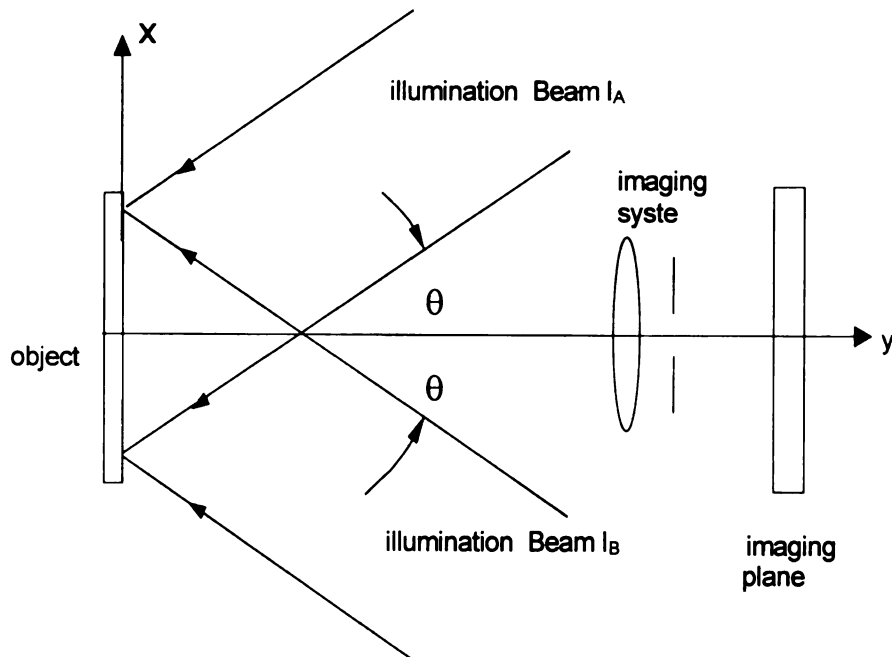
Figure 2.2. A simple in-plane speckle interferometer.

The intensity at any point of the speckle pattern can be written as:

$$I = I_A + I_B + 2\sqrt{I_A I_B} \, Cos\phi \qquad (2.3)$$

where I is the resultant intensity at the given point;

I_A is the intensity of beam 1;

I_B is the intensity of beam 2;

ϕ is the phase difference between beam 1 and beam 2.

As the speckle moves along the x-axis together with the object surface, the path length difference between the two illumination beams changes. Therefore, the relative phase difference ϕ between the two illumination beams is varied, and consequently the resultant intensity of the speckle varies. The speckle variation contains the information about the local displacement of the object surface.

Once a displacement occurs, the speckle intensity changes to:

$$I' = I_A + I_B + 2\sqrt{I_A I_B} \, Cos(\phi + \Delta\phi) \qquad (2.4)$$

where $\Delta\phi$ is the phase change induced by the movement of the speckle.

Let d_x represent the surface displacement in the x direction shown in Figure 2.2, the phase change is given as (Cloud, 1995):

$$\Delta\phi = \left(\frac{4\pi}{\lambda}\right) d_x \sin\theta \qquad (2.5)$$

where θ is the incidence angle of the illumination beams; λ is the wave length of the light.

In equation 2.4, when $\Delta\phi = 2n\pi$, (n=0,1, 2, 3...), maximum correlation happens between

I and I′. The correlation becomes zero when $\Delta\phi = (2n+1)\pi$, (n=0,1, 2, 3...). On the whole

field of the image, the speckle pattern is random, but the phase change ($\Delta\phi$) will be

smoothly varying.

Considering equation 2.5, the maximum correlation is along the lines where

$$d_x = \frac{n\lambda}{2\sin\theta} \tag{2.6}$$

and zero correlation is along the lines where

$$d_x = \frac{(n+1)\lambda}{2\sin\theta} \tag{2.7}$$

Variations of the speckle pattern correlation between I and I′ over the entire image appear

as a fringe pattern. If I′ is subtracted from I, which is commonly done, dark fringes occur

along the lines where $d_x = \dfrac{n\lambda}{2\sin\theta}$. Figure 2.3 presents an example of a fringe

pattern from speckle pattern correlation interferometry.

Equation 2.5 indicates that the local displacement information of the object is

contained in the phase change indicated by the interference at each speckle pattern.

Therefore, speckle pattern interferometry can be used to measure displacement point by

point, meaning that the formation of the fringe pattern of the speckle correlation is not

necessary to deduce the displacement information of the object.
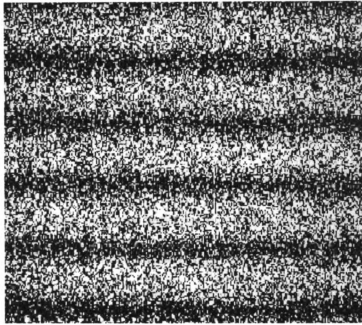
Figure 2.3. A fringe pattern of speckle pattern.

2.4 DSPI technique

Equation 2.1 shows that the size of speckles can be controlled by the F number of image lens. The minimum speckle size is generally between 5 and 100μm (Cloud 1996, Hong, S. S. 1997). It was soon realized that speckle pattern interferometry could be performed by electronic means such as video camera, electronic signal processing, and computer techniques, thereby increasing its accuracy and speed of measurement. This technique came to be known as electronic speckle pattern interferometry (ESPI). The major advantage of ESPI is that it enables real-time measurement of a surface displacement field without photographic processing. This advantage makes ESPI a good technique to form correlation fringe maps and perform non-destructive evaluation

qualitatively. However, the requirements to locate the center of fringes and number the fringe order make it unsatisfactory for quantitative measurement.

When a phase-shifting technique is introduced into speckle pattern interferometry, the phase and displacement information can be retrieved point by point without forming an interference fringe pattern. The application of phase shifting techniques makes ESPI a convenient quantitative technique.

With the advantages of digital techniques, various data processing steps can be done through digital methods inside a computer rather than in analog devices. When the computer takes over the role of processing all signals in the digital domain, The ESPI technique is alternatively termed digital speckle pattern interferometry (DSPI).

2.5 Phase shifting technique

If the relative phase ϕ can be computed both before and after deformation, the phase change $\Delta\phi$ at the speckle can be calculated by the subtraction between ϕ_{before} and ϕ_{after}; furthermore, the displacement can be determined at this point quantitatively. That is the objective of the phase shifting technique: to quantitatively determine phase value ϕ.

There are three unknowns in the intensity equation of speckle:

$I = I_A + I_B + 2\sqrt{I_A I_B} Cos\phi$, namely the beam one intensity I_A, beam two intensity I_B, and the relative phase ϕ between these two illumination beams. Obviously, a minimum of three equations is needed to determine the unknowns. Well-known phase shifting techniques can be used to quantitatively determine the phase value ϕ. Several phase

shifting algorithms have been developed by researchers, including the three-step technique, Carré technique, max-min scanning technique, etc. The main idea is to introduce some known or unknown phase changes artificially to get several additional intensity equations in order to derive the ϕ parameter. The equations may be generally expressed as

$$I_n = I_A + I_B + 2\sqrt{I_A I_B} Cos(\phi + \alpha_n)$$

where I_A is the intensity of beam one;

I_B is the intensity of beam two;

ϕ is the initial relative phase between the beams one and two;

α_n is the introduced phase shift;

n is the index of the phase shift step which is determined by the phase

shifting algorithm.

The final computation algorithm of phase value depends on the specific phase shifting parameters including the size and number of steps.

Commonly, the phase shifting technique uses some device, usually a mirror mounted on a piezoelectric transducer (PZT), to change the path length of one beam in an interferometer so as to induce some known phase changes in the interference. The corresponding intensities are recorded to derive the phase information point by point. Several different phase shifting algorithms were developed in the past years for DSPI. Dorrio, and Fernandez (1999) and Surrel (2000) categorized and reviewed these techniques in detail. Some algorithms are briefly introduced in the following sections.

2.5.1 Carré technique

In 1966, Carré developed a phase evaluation algorithm. Constant phase shift steps

$\alpha_n = -\dfrac{3}{2}\alpha, \; -\dfrac{1}{2}\alpha, \dfrac{1}{2}\alpha, \dfrac{3}{2}\alpha$ are introduced into equation 2.3 to obtain four speckle

patterns:

$$I_1 = I_A + I_B + 2\sqrt{I_A I_B}\,Cos\left(\phi - \frac{3}{2}\alpha\right) \qquad (2.8)$$

$$I_2 = I_A + I_B + 2\sqrt{I_A I_B}\,Cos\left(\phi - \frac{1}{2}\alpha\right) \qquad (2.9)$$

$$I_3 = I_A + I_B + 2\sqrt{I_A I_B}\,Cos\left(\phi + \frac{1}{2}\alpha\right) \qquad (2.10)$$

$$I_4 = I_A + I_B + 2\sqrt{I_A I_B}\,Cos\left(\phi + \frac{3}{2}\alpha\right) \qquad (2.11)$$

For this case, the phase can be computed as

$$\phi = \arctan\frac{\sqrt{[3(I_2 - I_3) - (I_1 - I_4)][(I_2 - I_3) + (I_1 - I_4)]}}{(I_2 + I_3) - (I_1 + I_4)} \qquad (2.12)$$

when α is near $\dfrac{\pi}{2}$, the intensity modulation, which is defined as the visibility of

speckles, is

$$\gamma = \frac{1}{2I_0}\sqrt{\frac{[(I_2 - I_3) + (I_1 - I_4)]^2 + [(I_2 + I_3) - (I_1 + I_4)]^2}{2}} \qquad (2.13)$$

where $I_0 = I_A + I_B$.

With this Carré technique, it is not necessary to calibrate the phase shifter to perform the above computations to determine phase value. However, since a constant phase step is assumed, the non-linearity of the phase shifter will affect the accuracy. Secondly, the α should be near $\dfrac{\pi}{2}$ in order to use the intensity modulation equation 2.13 to determine invalid pixels. Therefore, understanding of the properties of the phase shifter is still necessary to apply the Carré technique in reality.

2.5.2 Three-step technique

In equation 2.3, there are three unknowns I_A, I_B, and ϕ. Therefore, a minimum of three equations is needed to compute the unknowns. An example of three-step algorithm using $\dfrac{\pi}{2}$ step is,

$$I_1 = I_A + I_B + 2\sqrt{I_A I_B}\, Cos\,(\phi + \frac{1}{4}\pi) \tag{2.14}$$

$$I_2 = I_A + I_B + 2\sqrt{I_A I_B}\, Cos\,(\phi + \frac{3}{4}\pi) \tag{2.15}$$

$$I_3 = I_A + I_B + 2\sqrt{I_A I_B}\, Cos\,(\phi + \frac{5}{4}\pi) \tag{2.16}$$

Solving these three equations gives,

$$\phi = \arctan(\frac{I_3 - I_2}{I_1 - I_2}) \tag{2.17}$$

The intensity modulation is

21

$$\gamma = \frac{\sqrt{(I_1 - I_2)^2 + (I_2 - I_3)^2}}{2I_0}$$

where $I_0 = I_A + I_B$.

2.5.3 Four-step technique

A commonly used method is the four-step phase shifting technique. Equal $\frac{\pi}{2}$ phase

shifting steps are used in this algorithm.

$$I_1 = I_A + I_B + 2\sqrt{I_A I_B} Cos\ (\phi) \tag{2.18}$$

$$I_2 = I_A + I_B + 2\sqrt{I_A I_B} Cos\ (\phi + \frac{1}{2}\pi) \tag{2.19}$$

$$I_3 = I_A + I_B + 2\sqrt{I_A I_B} Cos\ (\phi + \pi) \tag{2.20}$$

$$I_4 = I_A + I_B + 2\sqrt{I_A I_B} Cos\ (\phi + \frac{3}{2}\pi) \tag{2.21}$$

The phase value is calculated by

$$\phi = \arctan(\frac{I_4 - I_2}{I_1 - I_3}) \tag{2.22}$$

The intensity modulation is

$$\gamma = \frac{\sqrt{(I_4 - I_2)^2 + (I_1 - I_3)^2}}{2I_0} \tag{2.23}$$

22

2.5.4 Seven-step technique

Several seven-step techniques were developed in the past decade (Zhang 1998, Larkin and Oreb 1992, De Groot 1995, Hibino, Oreb, Farrant, and Larkin 1995, Surrel 1996). The authors claimed these seven-step phase shifting techniques to be more insensitive to linear phase-shift miscalibration. One example among them uses

$$\alpha = (i-1)\frac{\pi}{2} \ (i=1,\ldots,7).$$

The phase is computed by

$$\phi = \arctan[\frac{-I_1 - 4I_2 + I_3 + 8I_4 + I_5 - 4I_6 - I_7}{I_1 - 2I_2 - 7I_3 + 7I_5 + 2I_6 - I_7}] \tag{2.24}$$

More detail about its derivation can be found in the references.

2.5.5 Max-min scanning algorithm

The Max-Min scanning method, was reported by Vikhagen (1990), Chen, Gramaglia, and Yeazell (2000), and Wang, Grant (1995). In this method, a set of recorded intensity signals is sorted to find the maximum and minimum intensity values at each pixel, and the phase angle is calculated from the obtained maximum and minimum intensities by the following equation.

$$\phi = ArcCos\left(\frac{I - \dfrac{I_{Max} + I_{Min}}{2}}{\dfrac{I_{Max} - I_{Min}}{2}}\right) \tag{2.25}$$

where I is the original intensity at one pixel, I_{Max} and I_{Min} are the maximum and minimum values of the intensity at the same pixel position as I.

Additional sign images are recorded by a small phase step to determine the sign of the calculated phase value. However, because of the discontinuity of the signal recording, this algorithm may miss the real maximum and minimum intensity values, causing uncertainties in the calculated results. Furthermore, to obtain the sign images, additional phase steps are needed, which is time consuming and requires accurate small phase steps.

2.5.6 Sinusoidal fitting technique

A sinusoid least square fitting method was reported by Ransom and Kokal (1986), Macy, and Bokor (1983). In the sinusoid fitting method, a number of intensity data are recorded during the phase shifting procedure. The intensity wave is assumed to be a sinusoidal waveform. The fitting model $I(v) = a(v) + b(v)\cos\phi(v)$ is used to fit the recorded signals. After solving a series of equations, parameters, a(v), b(v) and ϕ(v) are determined, where $\phi(v)$ is the phase value. This method was generally used to process 2-D fringe maps, which can be classed into spatial techniques for phase determination.

2.5.7 Comparison of phase shifting techniques

The Carré, three-step, and four-step techniques are simpler to implement than the others. But non-linearity and miscalibration of the phase shifter movement will cause errors in the computed results. Compared with the others, the seven-step, Max-min scanning, and sinusoidal techniques have been claimed to present better tolerance to the above errors. However, these algorithms require more complex mathematics work and computing time. There are some other techniques to retrieve phase information. The author could not list them all.

2.6 Image processing

Once the phase maps are determined before deformation and after deformation, the phase maps contain some noise. Therefore, some digital processing techniques are needed to remove errors and smooth the maps.

2.6.1 Phase change map

Equation 2.5 yields

$$d_x = \frac{\lambda \Delta \phi}{4\pi \sin \theta} \qquad (2.26)$$

where $\Delta \phi$ is the phase change caused by the displacement of the object surface. Therefore, once the $\Delta \phi$ is determined, the corresponding in-plane displacement can be computed.

In section 2.5, it is shown that phase values can be determined point by point through phase shifting techniques. After performing the phase shifting technique, both before deformation and after deformation, phase values are determined as ϕ_{before} and ϕ_{after}.

Phase change is

$$\Delta \phi = \phi_{after} - \phi_{before} \qquad (2.27)$$

Once the above procedure is employed pixel by pixel over the entire region of interest on the image, a phase change map is obtained. Figure 2.4 presents an example of a phase change map corresponding to some in-plane displacement of a rotated rigid body surface. Pepper-salt noise can be seen on this picture.

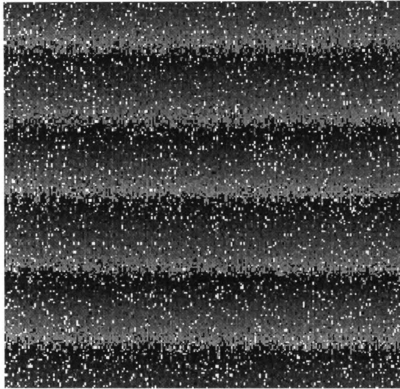Figure 2.4. Phase change map with errors.

2.6.2 Image filtering

When the phase shifting technique is performed in electronic speckle pattern interferometry, there are two main sources for noisy data points: slight decorrelation of speckles after deformation, and low intensity modulation as the phase is shifted. During signal processing, noisy points are generally marked as invalid pixels. To remove most of

the invalid pixels, the modulation of intensity at each pixel is checked to determine whether the point is good. If the calculated modulation is smaller than a given threshold during the phase shifting, the pixel is marked as an invalid pixel. The threshold value can be determined by trying different numbers until the best phase map is obtained. This type of work is very experience- related. These invalid pixels usually show up as pepper-salt noise in a phase change map, as seen in Figure 2.4. It is well known that a median window can effectively fill in these pepper-salt points (Hong 1997). To smooth pixel points where slight decorrelation occurs, a smoothing window can be employed which uses neighbor pixels to correct the center one in the window. Hence, a good phase change map can be generated, as seen in Figure 2.5.
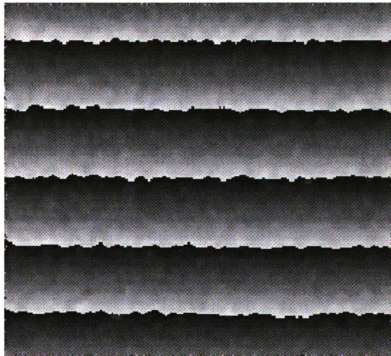

Figure 2.5. The phase map after smoothing of Figure 2.4 map.

2.6.3 Phase unwrapping

With the phase computation from the phase shifting technique, the phase can be determined to modulo 2π. After subtraction between the phase maps determined before and after deformation to obtain the $\Delta\phi$, it is obvious that the phase change map contains 2π ambiguities. The 2π ambiguities present 2π edges in a phase change map, which can be seen in Figure 2.5.

In order to determine the real displacement of each pixel from the phase change map, the 2π ambiguities must first be removed from the phase change map. Various phase unwrapping techniques have been developed to remove the 2π jumps that occur in the computed phase change map, so that a continuous phase change map can be obtained. These methods can be classified as: (1) Local phase unwrapping techniques, and (2) global phase unwrapping techniques.

The following is a brief summarization of some possible options that can be used.

The simplest phase unwrapping method is just an application of the classical one-dimensional phase unwrapping idea. A reference point is chosen to begin the unwrapping procedure. A horizontal line (or a vertical line) of pixels are scanned. Whenever a change more than a threshold π occurs between adjacent pixels, a 2π offset is added to (or subtracted from) the second pixel until there is no more than a π difference between all adjacent pixels along the line. Using the unwrapped line as the reference, the one-dimensional unwrapping procedure is then performed along all the vertical lines (horizontal lines). Finally, the phase ambiguities are removed from the entire image.

Figure 2.6 shows an example of an unwrapped phase map, which was obtained by performing this method on Figure 2.5.
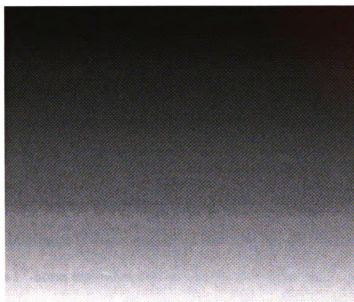
Figure 2.6. Unwrapped phase map of Figure 2.5.

When a noise-free phase map is available, this method is very ideal to perform phase unwrapping. However, noise pixels inevitably exist on phase map. Any noise in the image will generate an error that propagates along the unwrapping direction. Hence, a localized noise can affect a whole line of pixels, which typically turns out to cause a path dependent, global error.

A local phase unwrapping method was developed by Hong (1997). In this method, an n×n window is used to pick regions on which to perform phase unwrapping. In this window, the numbers of pixels that are above a given upper-threshold and those that are below a lower-threshold are counted separately. A $2n\pi$ offset is added to those low-

threshold pixels to remove the edge when the upper-threshold number is greater than the low-threshold number. On the other hand, a $2n\pi$ offset is subtracted from those upper-threshold pixels when the opposite condition is true. Also, the number of noise pixels is counted. If this number exceeds half of the entire pixels over a window that is $n \times n$, the pixel elements remain invalid. The advantage of this algorithm is that it is a path-independent local technique. So, the local noise does not expand to other regions. It must be pointed out that this local phase unwrapping method can be used to compute the strain field from phase change maps directly.

Based on the well known least-square method, an efficient phase unwrapping algorithm, the minimum L^P-norm algorithm, was reported by Ghiglia and Romero (1996). This minimum L^P-norm algorithm determines the unwrapped phase field by solving the discrete function of the wrapped and unwrapped phase fields. For more detailed information, refer to Ghiglia and Romero (1996). Furthermore, as reported by Kaufmann et al (1998), some numerical simulations showed that this algorithm can handle high densities of inconsistent pixels, objects with edges and holes when the order $p=0$. With this algorithm, some complex equations need to be solved and several weighting parameters need to be determined, which results in this being a time-consuming method.

Strand and Taxt (1999) evaluated the performance of several two-dimensional phase unwrapping algorithms with respect to correct unwrapped phase results and execution time. Comparisons of experimental results indicated that, in diverse noise conditions, there is always a trade-off between the efficiency and the amount of time needed to choose the most appropriate method.

In the past several years, new phase unwrapping algorithms have appeared at a rapid rate (e.g. He 2002, Herráez 2002, Huang, and Lai 2002, Gens 2003).

2.7 Displacement and strain computation

Once the phase change map is computed through the previous techniques, the in-plane displacement field can be determined by

$$d_x = \frac{\lambda \Delta \phi}{4\pi \sin \theta}$$
(2.28)

where d_x is the displacement;

λ is the wave length of illumination;

θ is the angle of illumination;

$\Delta \phi$ is the phase change caused by the displacement of the object surface

The illumination angle will affect the sensitivity of the measurement. As will be discussed in the next section.

If only the displacement field is desired, no further processing is necessary. However, a strain field is often demanded in mechanics analysis. It is obvious that the strain field can be determined by the first derivative of the displacement map. The least square fitting method is commonly used to compute the derivatives of the discrete data set.

The idea is to find a polynomial fitting function of the displacement field by the least square technique and to compute the derivatives of the fitting plane.

For an n×n window, let $u_{i,j}$ represent the displacement value in this window obtained from the previous steps, where i,j=1…n. A linear fitting plane for a 2-D field can be written as

$$U(x, y) = ax + by + c \qquad (2.29)$$

where the a, b, and c are three fitting parameters. The least square method minimizes the difference between the fitting data and the test results by the following equations.

$$\varepsilon = \sum_{i=1}^{n} \sum_{j=1}^{n} (U(x_{i,j}, y_{i,j}) - u_{i,j})^2$$

$$= \sum_{i=1}^{n} \sum_{j=1}^{n} (ax_{i,j} + by_{i,j} + c - u_{i,j})^2 \qquad (2.30)$$

The partial derivatives with respect to a, b, and c are set to zero to minimize the ε. After derivations, the following equations are obtained

$$a = \frac{\displaystyle\sum_{i=1}^{n} \sum_{j=1}^{n} x_{i,j} u_{i,j}}{\displaystyle\sum_{i=1}^{n} \sum_{j=1}^{n} x_{i,j}^2} \qquad (2.31)$$

$$b = \frac{\displaystyle\sum_{i=1}^{n} \sum_{j=1}^{n} y_{i,j} u_{i,j}}{\displaystyle\sum_{i=1}^{n} \sum_{j=1}^{n} y_{i,j}^2} \qquad (2.32)$$

$$c = \frac{\displaystyle\sum_{i=1}^{n}\sum_{j=1}^{n} u_{i,j}}{n^2} \qquad (2.33)$$

From equation 2.29, the a is the spatial derivative of the displacement map in the x direction, meaning it is the strain in x direction. The b is the strain in the y direction.

2.8 Sensitivity and spatial resolution of DSPI

The sensitivity is a key factor for the choice of an experimental measurement technique. The sensitivity of the DSPI technique depends on the spatial resolution limit of the image system and the illumination angle.

The sensitivity of the correlation fringes can be computed by

$$d_s = \frac{\lambda}{2\sin\theta} \qquad (2.34)$$

where d_S is the sensitivity of the fringes;

θ is the illumination angle;

λ is the wave length of the beam, which is 633nm for Helium-Neon laser.

For 8-bit, 256 gray levels image processing, the measurement sensitivity of DSPI is $d_S/256$ in theory (Hong 1997). The bigger the illumination angle, the higher the sensitivity.

The size of the speckle and the resolution of the imaging system determine the

maximum spatial resolution of DSPI setups (Equation 2.2).

The actual sensitivity of the measurement requires some experimental calibrations.

2.9 Practical DSPI setup

There are two typical applications of DSPI technique: to measure in-plane

displacement field and to measure out-of-plane displacement field.

Figure 2.7 presents a commonly used in-plane-sensitive arrangement of DSPI.
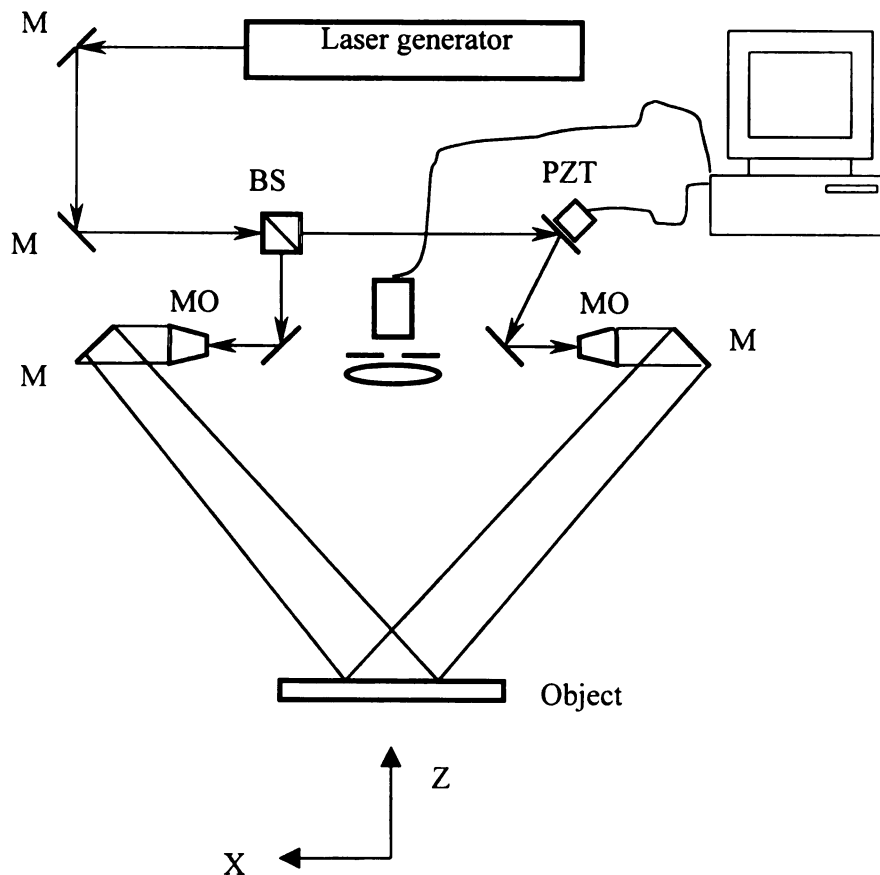

Figure 2.7. A typical in-plane sensitive DSPI system.

(M=mirror, BS=Beam splitter, MO=microscope object)

In figure 2.7, after the Helium-Neon laser generator, a beam splitter is used to obtain two coherent beams so that they can interfere with each other. A phase shifter, which is a mirror mounted on a piezoelectric transducer, is placed in one beam path. The driving voltage is controlled by the computer to vary the path length of the beam to perform the phase shifting. Spatial filters and microscope objectives are used to filter and expand the two beams to illuminate the object's surface. A CCD camera is used to record the speckle patterns. Recorded images are sent to the computer to perform signal processing.

If the setup is arranged so that one illuminating beam is directed into the camera and combined with the other object beam as a reference beam, this in-plane sensitive DSPI is changed into an out-of-plane sensitive DSPI setup.

Within the computer, proper algorithms, image capture, phase shifting, image filtering, phase unwrapping, displacement and strain field computation techniques are implemented to obtain the final quantitative results as needed.

Chapter 3. IMMS technique

3.1 Introduction

The phase shifting technique is a powerful tool to determine the phase angle for interferometric optical measurements such as moire, speckle interferometry and speckle shearing. As mentioned in Chapter 1, many phase shifting algorithms have been developed by Creath (1985), Sesselmann et al. (1998), Thesing (1998), Zhang, et al. (1998), Koliopoulos (1996), and Hibino (1999), among others. Complete and detailed classifications and descriptions of phase shifting algorithms were presented by Dorrio and Fernandez (1999) and Surrel (2000). In Chapter 2, some phase shifting techniques were briefly introduced. One of them, the Max-Min scanning method, was proposed a decade ago by Vikhagen (1990). In this method, a set of recorded intensity signals is sorted to find the maximum and minimum intensity values at each pixel, and the phase angle is calculated from the values obtained. Additional sign images are recorded both before and after deformation by use of tiny constant phase steps to determine the sign of the calculated phase value (Vikhagen 1990, Chen, et al 2000, Wang, et al 1995). However, because of the discontinuity of the signal record, the sorting of the recorded signal sequences may miss the real maximum and minimum intensity values, causing uncertainties in the calculated results. Furthermore, to obtain the sign images, additional phase steps are needed both before and after deformation, which requires accurate phase steps and is time consuming.

This chapter develops a new signal-processing algorithm for the Max-Min scanning method for phase determination. This new method will be named the Improved Max-Min Scanning phase determination method (IMMS). In this algorithm, the acquisition and processing of data are improved by employing a curve fitting technique to establish the waveform of the light intensity obtained from recorded signals. From this curve, the maximum and minimum intensity values are determined and the phase angle is computed. The sign of the phase can also be determined directly from this curve. Advantages of this approach include improved data processing efficiency and accuracy of the result. There is no need to acquire additional images to determine the sign of the computed phase angle. In addition, calibration of the phase shifter is not required, and, in certain instances, the phase shifting device can be eliminated entirely from the setup.

Phase shifting is a key step in optical measurement. There is always a big concern about the environmental tolerance of all kinds of phase determination techniques, because the noise tolerance determines the requirements for the working conditions of the techniques. In other words, the noise tolerance establishes limitations for the application of the phase shifting techniques. The majority of current techniques require a vibration-insulated table in order to work. In this chapter, employment of low-pass filtering and curve fitting techniques to the recorded signals in the time domain is shown to improve the noise tolerance of the developed IMMS method. Numerical simulations and tests are presented.

3.2 The Principle of the IMMS method for phase determination

3.2.1 Mathematical Development

In this chapter, the in-plane-sensitive speckle pattern interferometer is used to explain the derivation of the new signal-processing algorithm. The final result of this chapter can be applied to the out-of-plane sensitive interferometer as well as other interferometers that require a phase shifting technique. To illustrate the theoretical derivation of the new algorithm, suppose that an object is illuminated by two coherent laser beams I_1 and I_2, as shown in Figure 3.1. A speckle pattern is constructed both on the surface of the object and on the sensor part of the imaging system.
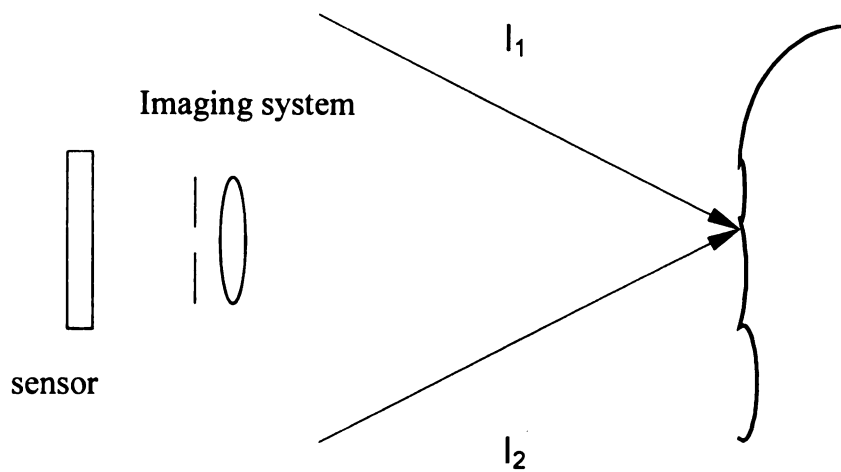
Figure 3.1. Object illuminated by two beams.

According to the well known optical theory as summarized in section 2.3 of the previous chapter, at each point of the image area, the intensity of the speckle interference can be expressed by the following equation

$$I = I_1 + I_2 + 2\sqrt{I_1 I_2} Cos \phi \qquad (3.1)$$

where I is the resultant intensity;

I_A is the intensity of beam 1;

I_B is the intensity of beam 2;

ϕ is the phase difference between beam 1 and beam 2.

In this equation, there are three unknowns, I_1 , I_2 and ϕ. Among them, the phase ϕ is the key parameter that is the goal of the phase determination techniques, because the change of this phase angle during deformation is the container of the displacement information at each speckle point.

From equation (3.1), it is known that the intensity I is a cosine function of the relative phase difference between the two interfering beams, which means that the intensity I is a cosinusoidal waveform. Furthermore, the $I_1 + I_2$ represents the background of the speckle, and the $2\sqrt{I_1 I_2}$ represents the visibility of the speckle point. In this equation, when $\phi = 2n\pi$, n = 0, 1, 2, ... , the resultant intensity I reaches the maximum value:

$$I_{Max} = I_1 + I_2 + 2\sqrt{I_1 I_2} \qquad (3.2)$$

When $\phi = (2n+1)\pi$, n= 0, 1, 2, ..., the intensity I reaches the minimum value:

$$I_{Min} = I_1 + I_2 - 2\sqrt{I_1 I_2} \qquad (3.3)$$

Adding (3.2) and (3.3) gives

$$I_{Max} + I_{Min} = 2(I_1 + I_2) \qquad (3.4)$$

so

$$I_1 + I_2 = \frac{I_{Max} + I_{Min}}{2} \qquad (3.5)$$

which is the average intensity value or the background of the intensity wave. Subtracting

(3.2) and (3.3) gives

$$I_{Max} - I_{Min} = 4\sqrt{I_1 I_2} \qquad (3.6)$$

and

$$2\sqrt{I_1 I_2} = \frac{I_{Max} - I_{Min}}{2} \qquad (3.7)$$

This is the amplitude or the visibility of the intensity wave.

Substitute equations. (3.5) and (3.7) into equation (3.1) to obtain

$$I = \frac{I_{Max} + I_{Min}}{2} + \frac{I_{Max} - I_{Min}}{2} Cos\phi \qquad (3.8)$$

which yields

$$Cos\phi = \frac{I - \dfrac{I_{Max} + I_{Min}}{2}}{\dfrac{I_{Max} - I_{Min}}{2}} \qquad (3.9)$$

Therefore, the phase can be computed as

$$\phi = ArcCos\left(\frac{I - \dfrac{I_{Max} + I_{Min}}{2}}{\dfrac{I_{Max} - I_{Min}}{2}} \right)$$ (3.10)

where I is the original intensity at one pixel, and I_{Max} and I_{Min} are the maximum and minimum values of the intensity at the same pixel position as I. Once I_{Max} and I_{Min} are determined, then, from equation (3.10), ϕ can be determined in the range between 0 and π.

A second key step is to determine in which quadrant to place the phase. Taking the derivative of equation (3.1) yields

$$\frac{dI}{d\phi} = -2\sqrt{I_1 I_2} \, Sin\,\phi$$ (3.11)

Then

$$Sin\phi = -\frac{\dfrac{dI}{d\phi}}{2\sqrt{I_1 I_2}}$$ (3.12)

The sign of $\dfrac{dI}{d\phi}$, which is opposite to the sign of $Sin(\phi)$, can be used to determine the quadrant in which the phase ϕ is located, as shown in Table 3.1.

Table 3.1. Quadrant determination of ϕ by signs of $\mathrm{Cos}\phi$ and $\dfrac{dI}{d\phi}$.

$\mathrm{Cos}\phi$	$\dfrac{dI}{d\phi}$	Quadrant of ϕ
+	+	Quadrant 4
+	-	Quadrant 1
-	+	Quadrant 3
-	-	Quadrant 2

3.2.2 Algorithm to determine I_{Max}, I_{Min} and ϕ.

The question of how to find I_{Max} and I_{Min} still remains. As mentioned before, the intensity I has the cosinusoidal waveform shape. Therefore, if several cycles of the intensity wave can be obtained at one pixel, the I_{Max} and I_{Min} are easily determined from the waveform at this point. In our experimental setup, a PZT phase shifter is used to artificially change the path length of one beam so that the phase difference between the two interfering beams is changed. A computer is used to record digital pictures of the light intensity of the speckle image for each mirror location. The Nyquist theorem must be fulfilled to sample the intensity waveform. To minimize the chance that the intensity

background and the fringe visibility will change, the signal recording should be finished in a short time, as soon as possible. After recording, at each image point, the light intensity values are plotted against the driving voltages of the PZT, and a low-pass filter and least-square curve fitting method are used to process the test values to obtain a good intensity changing waveform. For low pass filter and curve fitting techniques, a large number of complex mathematical equations need to be solved. Fortunately, many commercial software packages are capable of doing this processing, making it easy to develop an efficient program. Since only the intensity waveform instead of the fitting parameters is needed to determine I_{Max} and $I_{Min,}$ there are more options for commercial software to do curve fitting. In the LabVIEW environment used here, a linear low pass Butterworth filter is used to filter noise (National Instrument Corporation, 1998). Because the intensity waveform is not purely cosinusoidal, a general polynomial curve fit of 10th –order is used to fit the recorded signals at each image pixel. A smooth intensity waveform is obtained. Figures 3.2 and 3.3 show an example of such an intensity wave at one point on a test specimen before and after curve fitting. On the fitting curve, the derivative at each point is computed to find the local maximum and minimum intensity values. The average of all local maximum intensities is counted as the I_{Max} , and the average of all local minimum intensities is counted as the I_{Min} . By substituting these parameters into equation (3.10), the phase ϕ can be calculated.
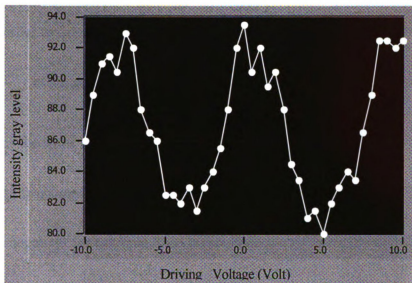
Figure 3.2.   An example of intensity wave obtained by phase shifting.
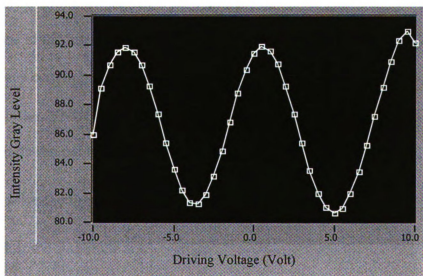

Figure 3.3. Waveform of Fig. 3.2 after curve fitting.

In order to determine the quadrant of the obtained phase, the derivative of the fitting

curve $\dfrac{dI}{dV}$ at the point where the driving voltage equals zero is computed. Obviously,

$\dfrac{dI}{dV}$ has the same sign as $\dfrac{dI}{d\phi}$. From table 3.1, if $\dfrac{dI}{dV}$ is positive, the sign of phase ϕ

obtained from equation. (3.10) is reversed to locate the phase angle in quadrant 3 or 4. If

$\dfrac{dI}{dV}$ is negative, for example, then ϕ should be placed in quadrant 1 or 2. The sign of

$Cos(\phi)$, already determined, establishes which of these two quadrants is the correct one.

After completing the above procedure at each point across the entire image field, the

phase map is determined modulo 2π. The 2π ambiguities can be removed by phase

unwrapping techniques discussed in Chapter 2 (Creath 1985, Sesselmann et al. 1998,

Kaufmann, et al. 1998).

This algorithm, which scans the intensity, has two potential difficulties: (1) if the

amplitude of the intensity wave is too small, the waveform will be blurred by noisy

signals at a certain point; (2) if the intensity value before phase shifting is not between the

I_{Max} and I_{Min}, which results in the value of the cosine equation being greater than 1, the

phase angle can not be calculated.

To solve the first problem, the amplitude $\dfrac{I_{Max} - I_{Min}}{2}$ of the waveform can be

checked. If the amplitude at a certain point is smaller than a given threshold value

determined by the user's experience, the point is marked as an invalid pixel. A big

threshold, which implies a high percentage of invalid pixels in the whole image, makes it

difficult, even impossible, to obtain a smooth phase map. A too-small threshold results in

a very rough phase map. The threshold can be determined by trying different numbers until the best phase map is obtained. In this work, amplitude 4 gray levels were employed as the threshold. To solve the second problem, the intensity value can be approximated by the nearest value that lies within the range of the intensity wave. However, if the value exceeds the intensity range considerably, the point is marked as an invalid pixel.

3.3 Experimental Examples

To verify the phase shifting algorithm presented above, the method was first applied in a digital speckle pattern interferometry (DSPI) setup to measure the crack tip position in a compact tension (CT) specimen (Cloud, Ding, and Raju 2002). Second, the in-plane displacement of a disk that was given a controlled small rotation was measured (Cloud 1995, 1979). For this purpose, a LabVIEW program was designed (National Instrument Corporation, 1998). This program acquires image data from a CCD camera pixel-by-pixel through a frame grabbing board (National Instruments, PCI-IMAG-1402), controls the PZT to implement phase shifting, calculates the phase at each pixel, and finally computes the displacement or the coordinates of the crack tip.

3.3.1 Determination of the Crack Tip Position

In this experiment, the setup that was used by Cloud, Ding, and Raju (2002) was used. The results obtained from the new algorithm were compared to those obtained by the Carré phase shifting technique in which $\pi /2$ phase shifts were used. Less than one minute on a PIII-500 PC served to finish signal processing of a 200×200 pixel region, and forty recorded images were used in the new algorithm. Figure 3.4 is a diagram of the specimen.
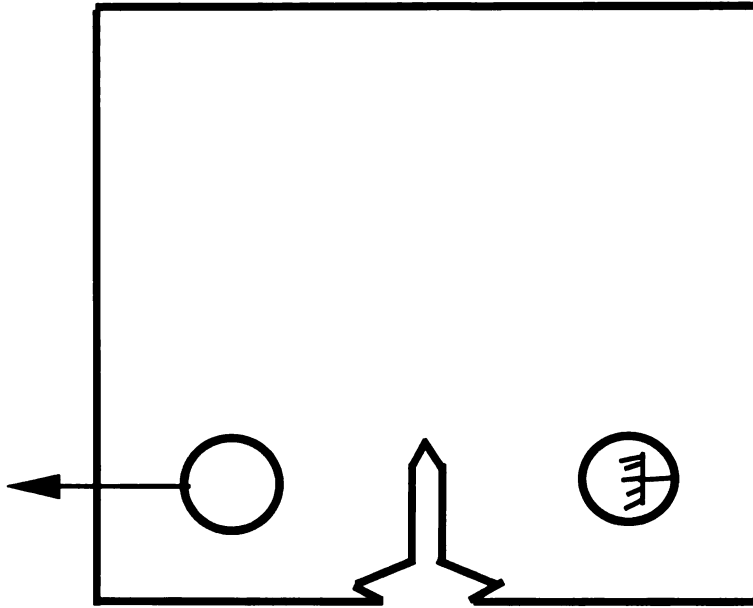
Figure 3.4. Load condition of CT specimen.

Figures 3.5 to 3.7 were obtained by the new algorithm. Figure 3.5 shows the raw phase change map with salt-and pepper noise. A 5×5 smoothing filter process (National Instrument Corporation 1998) was used to remove the noise and to obtain a smooth phase change map as seen in Figure 3.6. After performing phase unwrapping to remove 2 π ambiguities on phase change map, a continuous smooth phase map is seen in Figure 3.7. Figure 3.8 is the phase map after unwrapping obtained by using the Carré phase shifting method. The coordinates of the crack tip are indicated on the images (Figure3.7 and Figure 3.8). Through these coordinates, it was established that the crack tip positions determined by the two methods were in a good agreement. The new IMMS method works as well as the Carré phase shifting method in this application.
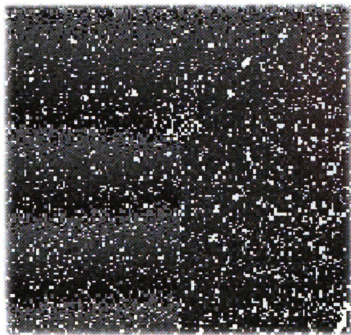
Figure 3.5. Raw phase change map.
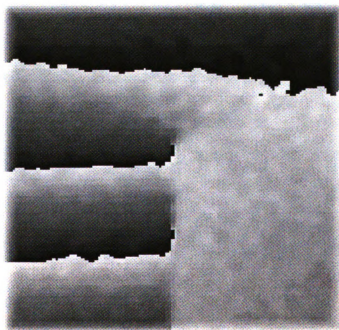
Figure 3.6. Phase change map after smoothing.
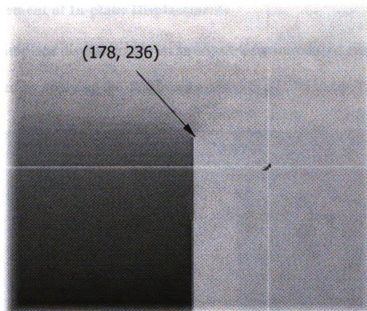
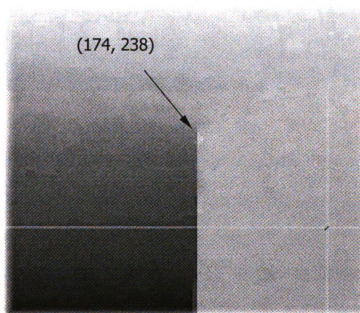Figure 3.7. Crack tip position from the new IMMS algorithm.

Figure 3.8. Crack tip position from the Carré method.

3.3.2 Measurement of In-plane Displacements

Known in-plane displacements on an object were introduced and compared with the results obtained by applying the developed method in a DSPI setup. A calibration device
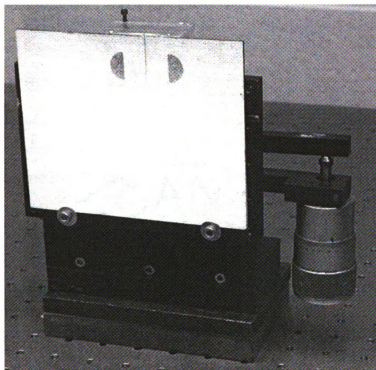

Figure 3.9. Calibration plate.

that uses a rigid plate that can be given known small in-plane rotation was used (Cloud 1995, 1979). The plate is rotated by using a micrometer that engages a lever arm that is 118 mm long as shown in Figure 3.9. Least reading of the micrometer is 0.0001 in (0.00254 mm). During the experiment, with small rotations of the plate, the expected horizontal correlation fringes were observed (Figure 3.10). Three random points on the surface of the rigid plate were chosen to compare the displacements obtained by this new algorithm with the known induced displacements. The comparative values and errors are

given in Table 3.2. The difference is within 4%. It can be said that the measured displacement results are in good agreement with induced displacement.
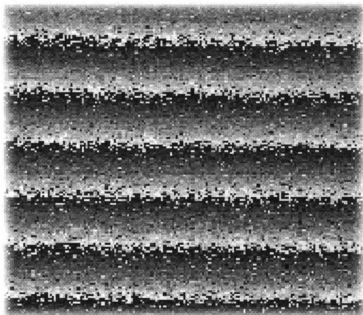

Figure 3.10. Correlation fringe map obtained by the new algorithm.

Table 3.2. Comparison of the in-plane displacements calculated by the new algorithm and induced displacements.

Rotating Angle(rad)	Induced Displacement(μm)	Measured Displacement(μm)	Difference
2.0532e-4	3.475	3.51	1.00%
2.7517e-4	5.866	5.64	3.85%
2.5400e-4	6.388	6.16	3.57%

The results of these two examples of applications of the newly developed IMMS algorithm indicate that the developed IMMS method for phase determination can work well to perform surface measurements in DSPI apparatus. However these two tests were performed with the DSPI setup and specimen mounted on vibration-insulated table that can minimize noise effects significantly. Therefore, the test results only mean that the new technique can work as well as other existing phase shifting techniques in a laboratory environment. The next concern is what advantages the new IMMS method has compared with other techniques for phase determination. The purpose in developing this new IMMS method is to improve the noise tolerance of the DSPI setup so that this non-contact technique for surface measurement is more practical for real application environments. In the next section, in order to verify the general objectives of this research work, the noise tolerance of the new method is tested by performing numerical simulations and real applications.

3.4 The noise tolerance property of the IMMS method

Since some numerical filters, for instance a low pass filter, can be employed in the algorithm to process the recorded intensity signals in the time domain, a good noise tolerance is expected for this new IMMS method. To verify this assumption, numerical simulations are the first simple choice to perform the test work. A second choice is to apply the new algorithm in some noisy work conditions. In this section, some experiments are presented to explore the noise tolerance properties of the IMMS method. The calibration plate shown in Figure 3.9 was used in this test. At ten points chosen randomly over the entire image, good intensity variation curves are recorded by driving the PZT mirror in an in-plane sensitive DSPI setup where the whole setup and specimen

are placed on a vibration insulated table. Numerical simulations and some real noise signals are used to test the noise tolerance property of this IMMS method at these ten points.

3.4.1 Numerical simulations

A white noise signal that includes wide band of frequency of noise is commonly used to perform environmental noise simulations. In this research work, a numerical Gaussian white noise generator that has capability to control the standard deviation of generated noise signals is used to generate some white noise signals. These noise signals are added to the recorded intensity signals. The IMMS method is employed to both the originally recorded intensity signals and to the noise-added intensity signals to determine phase values. Results are compared as in the following.

Figure 3.11 is a recorded good intensity waveform after removing the background intensity. Figure 3.12 is an example of Gaussian white noise whose standard deviation is 2.0. Figure 3.13 presents the intensity waveform with the Gaussian noise added on.
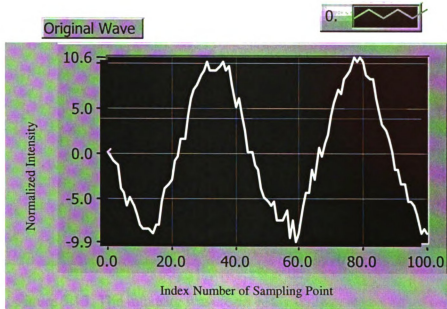
Figure 3.11. A recorded good intensity changing curve.
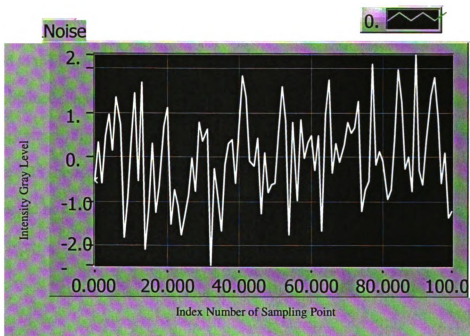

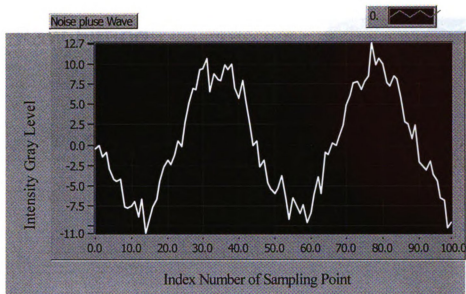Figure 3.12. Gaussian white noise signals.

Figure 3.13. The intensity waveform with Gaussian noise added on.

In this example, the RMS signal-to-noise ratio is 6.3. After performing the IMMS method to the Figures 3.11 and 3.13 individually, two final fitting intensity waveforms were obtained. Figure 3.14 presents the final fitting curve of the originally recorded intensity wave. Figure 3.15 shows the final result curve of noise-added intensity signals (Figure 3.13) obtained from IMMS. The results indicate that the effect of this Gaussian noise could be removed completely by the IMMS method.
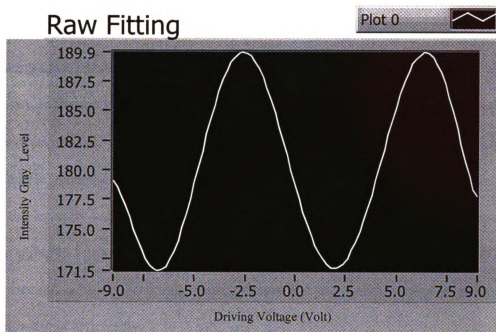
Figure 3.14. The fitting curve of the original recorded signals.
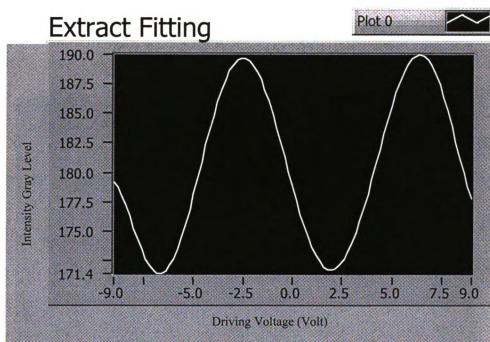
Figure 3.15. The fitting curve of noise-added intensity signals.

The deviation of the noise signals was increased gradually. One more example from among these extensive tests is reported. A Gaussian noise signal with higher deviation is shown in Figure 3.16. The deviation of this noise is 6.5, more than three times of the previous one that was at 2.0. The RMS signal-to-noise ratio is decreased to 0.96 in this example, meaning that the noise is nearly as large as the signal. Adding this noise signal to the intensity waveform (Figure 3.11) yields Figure 3.17, which is more chaotic than the signal in Figure 3.13. Figure 3.18 shows the IMMS result from Figure 3.17. Compared to Figure 3.14, this result indicates that the IMMS method cannot process this noisy signal efficiently.

By adjusting the deviation of the white noise signals, it is shown that the IMMS method can remove noise with a small deviation efficiently. Quantitatively, a noise that has an RMS signal-to-noise ratio larger than 1.8 can be processed successfully.
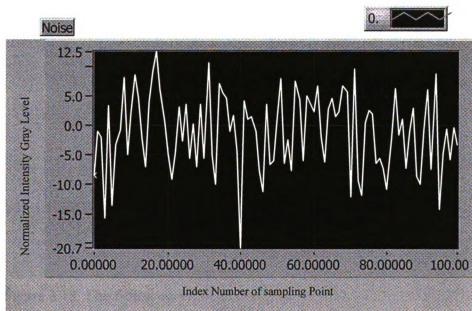

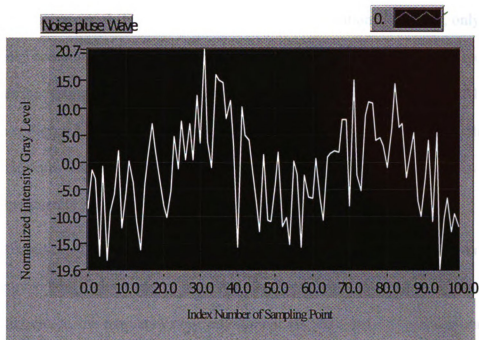Figure 3.16. Gaussian noise with a 6.5 deviation.

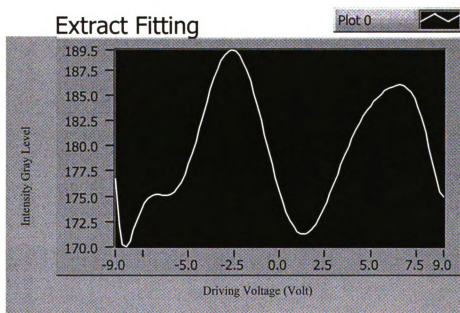Figure 3.17. Intensity waveform with the new noise added on.

Figure 3.18. The fitting curve of an intensity wave with a 6.5 deviation noise added.

58

In the next step, a high pass filter removes the low frequency components from the same very noisy signal (Figure 3.16), which has a 6.5 deviation. Therefore, only the high frequency components of the noise are left and added to the original signal. Figure 3.19 presents the resultant intensity waveform. The RMS signal-to-noise ratio is 1.21 in this example. Figure 3.20 shows that good results are obtained from the IMMS method. This result indicates that high frequency noise even with big amplitude can be removed by the IMMS efficiently.

Repetition of the simulation tests showed that the IMMS method gives very good immunity to both high frequency noise and small amplitude low frequency white noise. Large amplitude low frequency noise can damage the efficiency of the noise immunity of the IMMS method.
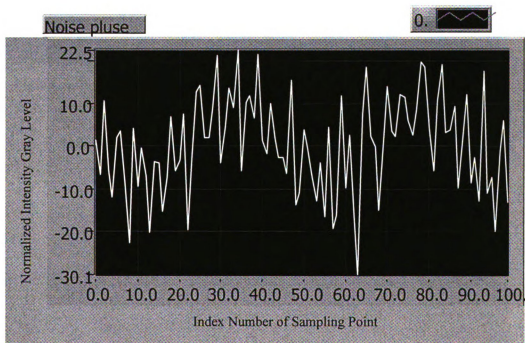

Figure 3.19. The intensity waveform with high frequency component of the noise added on.
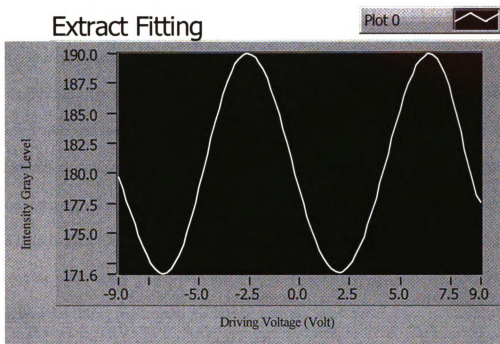
Figure 3.20. The fitting curve of the intensity wave with a 6.5 deviation high frequency noise added.

3.4.2 The effect of real noise signals

At various points on the specimen, intensity changes induced by environmental noise (such as air turbulence and vibration) were recorded under three different situations by DSPI setup and added to good intensity curves. The IMMS method was employed to process these noise-added signals.

A. The specimen was placed on a vibration-insulated table:

In this case, both the DSPI equipment and specimen were placed on a vibration-insulated table. At some pixels, the intensity changes induced by environmental noise were recorded. A noise signal example is shown in Figure 3.21. This noise was added to a good intensity waveform as shown in Figure 3.22. In this example, the RMS signal-to-noise ratio is 7.22. On this table, the vibration is minute. So, the RMS-SNR was bigger than for the other cases. The IMMS method was employed to process the data. Figure 3.23 gives the fitting result from the IMMS method. The phase value determined by the IMMS is –3.14 Rad, which exactly matches the phase obtained from the original signals. The figures and the match of the phase values indicate that the IMMS method works very well in this situation, as expected.
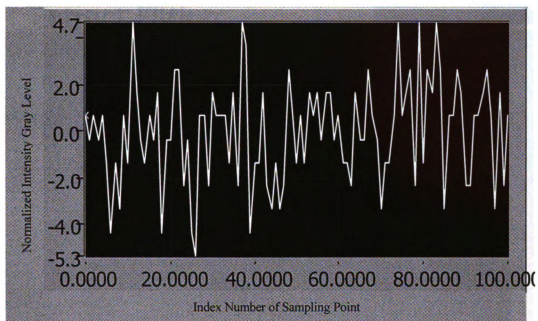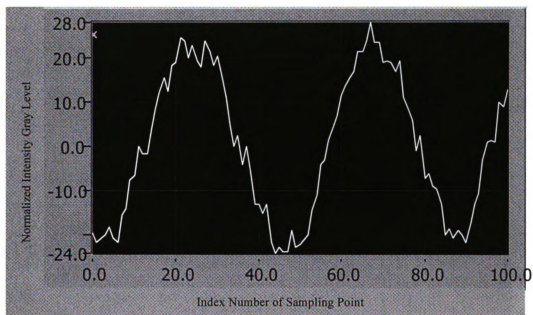
Figure 3.21. Noise signals under A condition.

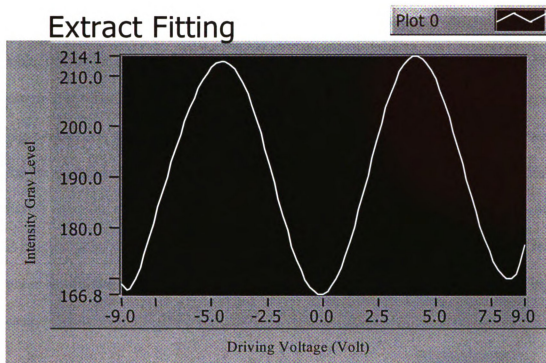Figure 3.22. Intensity change curve with noise added.

Figure 3.23. The fitting curve obtained by IMMS.

B. The specimen was put on the same table without air support vibration isolation:

In this case, the DSPI setup and the specimen were still on the vibration-insulated table, but the air was released from the supporting structure of the table. Figure 3.24 is an example of recorded noise signals under this situation. The amplitude of this noise was bigger than that of case A. The original intensity curve was distorted much more than in the previous case, as seen by comparing the sample photo of Figure 3.25 and Figure 3.22. In this situation, the specimen vibration was very serious. The RMS-SNR is 1.81, which is much smaller than in case A. Figure 3.26 shows the IMMS processing result. The phase results still match exactly at –2.29Rad. The IMMS method still works well in this case.
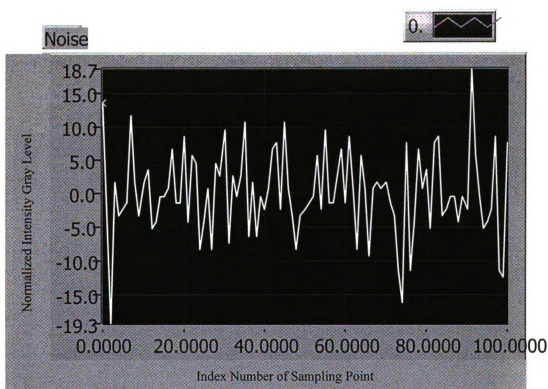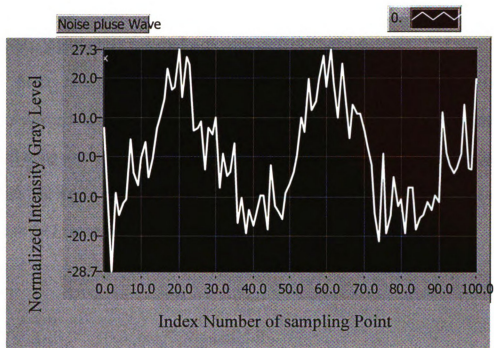

Figure 3.24. Noise signal.

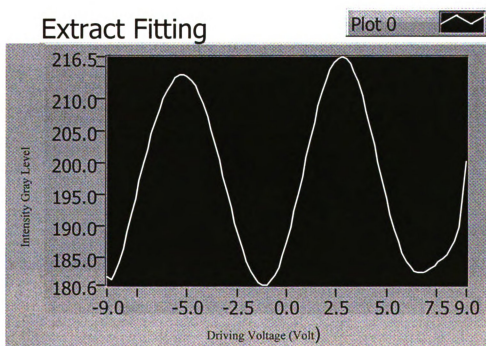Figure 3.25. Intensity curve with noise added.

Figure 3.26. The IMMS result.

C. Noise signals were recorded with the specimen placed on a cart.

In this case, the specimen was placed on an ordinary laboratory cart that is much more susceptible to environmental noise, especially the vibrations of the building. The DSPI setup was still located on the table. Real noise signals were recorded at various points and bigger variances than cases A and B were observed for these noise signals. Figure 3.27 shows one noise example.
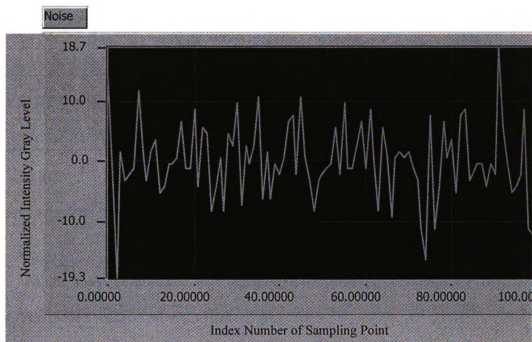

Figure 3.27. Noise sample obtained under case C.

In this situation, an alternative calibration method was used, measuring in-plane displacement of a plate. The recorded noise signals were added to each point over all the pixels in the image during displacement measurement by the IMMS algorithm. The same displacement calibration set up as shown in Figure 3.9 was used to introduce known in-plane displacement. Table 3.3 gives some examples of these test results. They indicate that the IMMS worked well even under these high noise conditions.

Table 3.3. Some examples of displacement measurements.

Variance of noise signals	Measured displacement by the IMMS (μm)	Induced known displacement(μm)	Percentage difference
30.62	1.85	1.86	-0.75
37.75	1.75	1.68	4.04
30.23	2.82	2.70	4.29

All the above simulations were repeated tens of times at different dates and times of day. The IMMS method proved to have a good ability to reduce some specific noise effects. Especially, the IMMS method has very reliable ability to remove high frequency noise and small amplitude low frequency noise. This ability can make the DSPI technique useful in more practical environments than before.

Chapter 4. A technique for calibrating and evaluating phase shifter

4.1 Introduction

As mentioned, a phase shifter is commonly used in DSPI setups to evaluate phase angle. The working status of the phase shifter, such as the necessary driving voltage, non-linearity, stability of the PZT, and tilt of the mirror, greatly affect the accuracy of the ultimate measurement results of the DSPI technique. Therefore, calibration of the phase shifter is a very important step in the DSPI technique. In the past decades, several methods were developed to calibrate the phase shifter. Two methods are commonly used. The first one is a fringe-tracking method and the second one is the Carré method as described by Brug (1999). These methods have some obvious drawbacks and limitations. The fringe-tracking method is suited only for accurate 2π phase steps and is difficult to control. The Carré method uses several phase-stepped images to calculate the phase shifting angle with an assumption that the phase shifter is linear. These techniques cannot evaluate the linearity, the tilt, and the non-uniformity of the motion of phase shifters.

Based on the IMMS technique, an online method to calibrate the phase shifter is developed here. This improved algorithm provides an easy and convenient way to inspect the linearity and the non-uniformity of the phase shifter. It is suitable to be used to check the working reliability of the phase shifting setup in real time.

68

4.2 Scanning method for PZT's calibration

As described in Chapter 3, after the determination of the maximum and minimum intensities I_{max} and I_{min}, the phase value can be computed by equation 3.10. The same computation can be applied at each point along the entire intensity curve. Therefore, the plot of phase values versus driving voltages was obtained with 2π ambiguities as seen in Figure 4.1. The real diagram of phases versus the driving voltage was obtained by performing phase unwrapping with respect to the zero driving voltage point. Figure 4.2 presents an example of a phase vs. driving-voltage diagram after phase unwrapping. The phase steps induced by the driving voltages can be determined from this diagram (Figure 4.2). For instance, on this sample curve, 2.5 volts to the PZT will result in a 2-radian phase shift. Furthermore, from this phase diagram, the driving voltage to the PZT to get a specified phase step at this pixel point can be obtained by interpolation of the obtained data. As well, the non-linearity of the phase shifting at this point is visually displayed on the curve. To calibrate a specific phase step, i.e. $\pi/2$ phase step, the above calibration can be performed at a number of pixel points over the entire image. An average driving voltage to get that phase step can be computed.
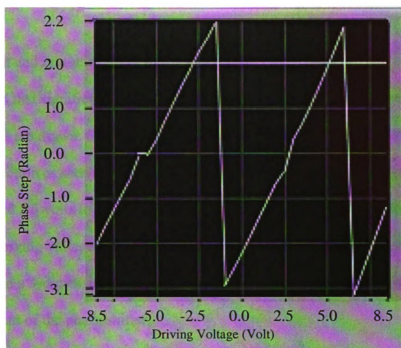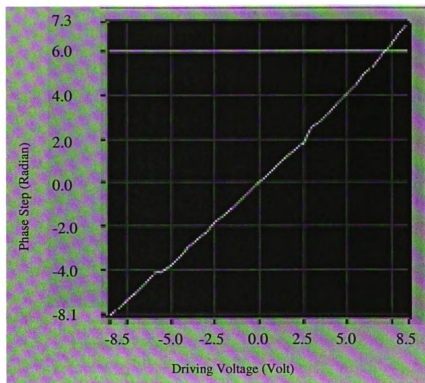
Figure 4.1. Phase step with 2π ambiguity.

Figure 4.2. Phase step V.S. driving voltage.

Tilt and non-uniformity of the phase shifter movement are two other important concerns that significantly affect the accuracy of phase shifting. In the illumination area, two lines are drawn. One is along the x-axis direction, and the other one is along the y-axis direction as seen in Figure 4.3. At a specific given driving voltage, such as the calibrated 2.5 volts to obtain a 2-radian phase step, phase shifting results corresponding to this driving voltage at all points along these two perpendicular edges of the image are plotted in a 3-dimensional graph to visually illustrate the tilt and non-uniformity of the movement of the phase shifter.
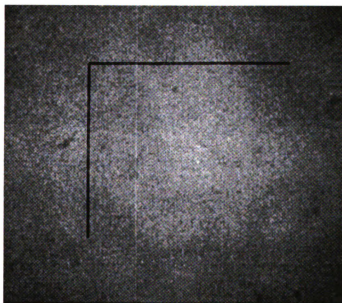

Figure 4.3. Two lines are drawn on the image.

To implement the idea, the IMMS signal-processing algorithm developed in Chapter 3 was employed to obtain the phase shifting curve at each point along these two edges. The phase shifting values corresponding to the calibrated $\pi/2$ driving voltage were determined from the fitting curve. The computed phase shifting values were plotted in a 3-D graph, on which the tilt and non-uniformity of the phase shifter can be inspected visually and directly. Figure 4.4 is an example of such a 3-D graph. After rotation of Figure 4.4, a 2-D side view of the Figure 4.4 was obtained as in Figure 4.5. On this 2-D graph, the trend line and the distribution of the phase shifting values indicate the tilt and uniformity of the phase shifting motion. For instance, if there is an angle between the trend line and horizontal line in the graph, it can be inferred that tilt occurs along this edge, the bigger the angle, the more serious the tilt. If the phase shifting value points are distributed far away from a straight trend line, we can say the uniformity of the phase shifting motion is bad. If all points concentrate on a straight trend line closely, the uniformity of the phase shifting motion is good. Therefore, Figure 4.5 can show the tilt and non-uniformity of the movement of the phase shifter along the x-axis direction clearly. Figure 4.6 is a 2-D side view along the vertical direction to show the tilt and non-uniformity of the phase shifter motion in the Y direction.
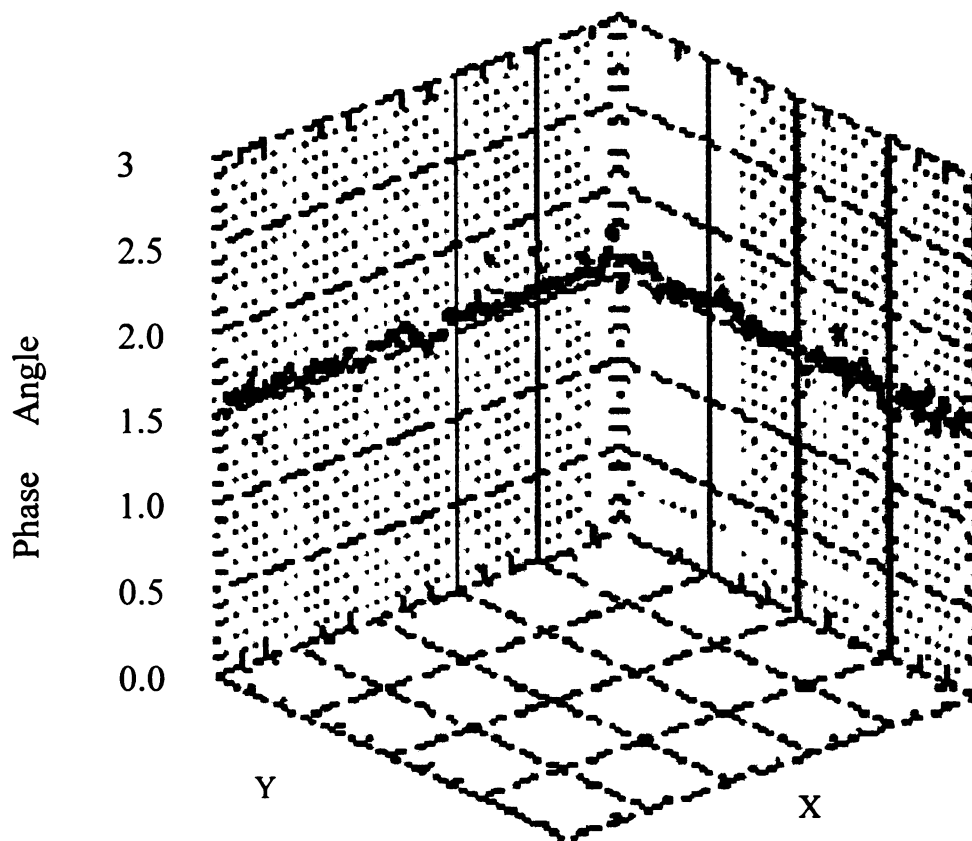
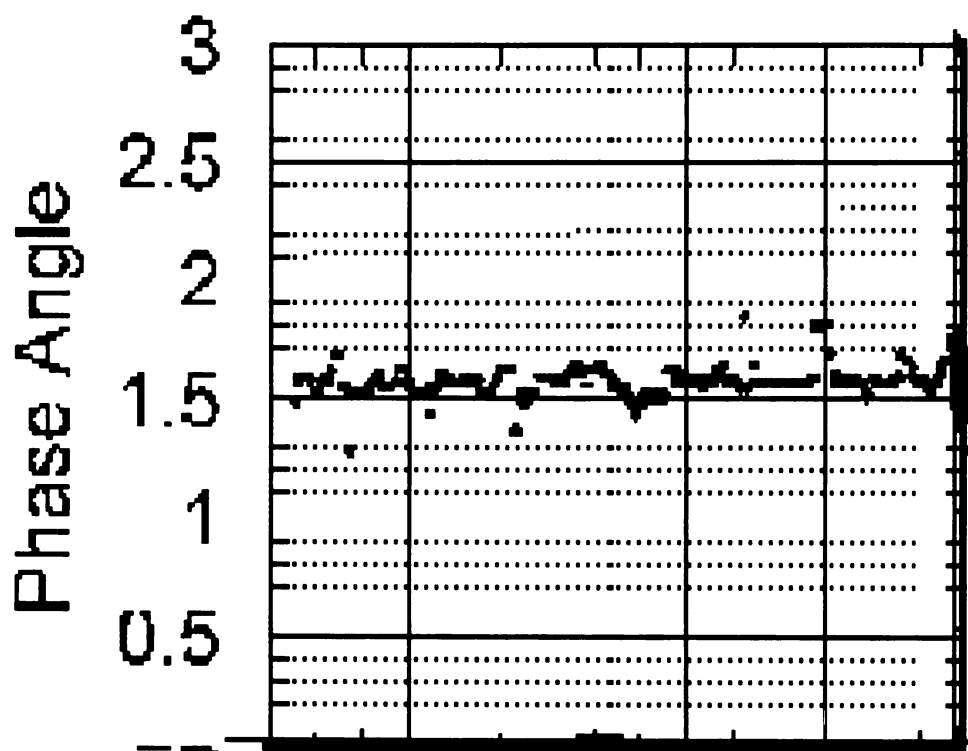Figure 4.4. A 3-D plot of the obtained phase shifting results.

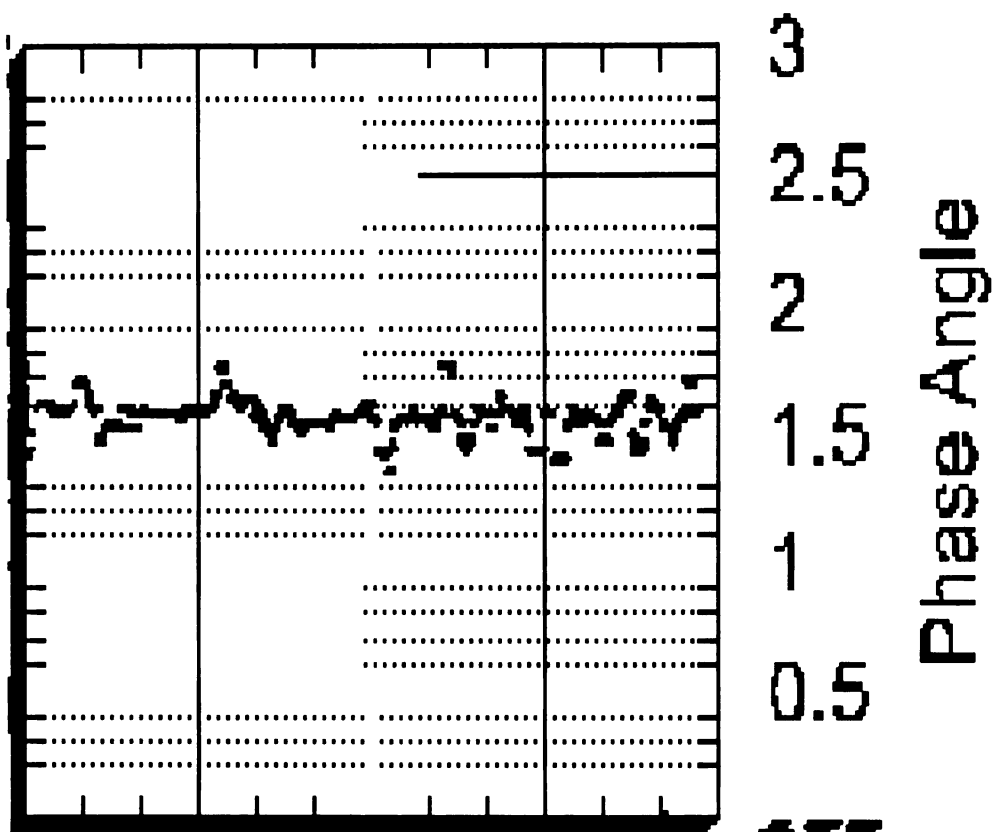Figure 4.5. Tilt and non- uniformity in x-direction.

Figure 4.6. Tilt and non- uniformity in y-direction.

4.3 Calibrations of two phase shifters

The method described above has been used to calibrate and inspect the phase shifter used in a DSPI setup, which is a small mirror mounted on a PZT.

Actually, the figures from 4.1 to 4.5 are from a calibration test of a real piezo electronic transducer phase shifter. This phase shifter is a small mirror mounted on a PZT. Figure 4.7 represents a recorded intensity wave. After filtering and curve fitting, a smooth waveform was obtained as shown in Figure 4.8.

The calibration result has been shown in Figure 4.2. For this specific experimental setup, the driving voltage to get $\pi/2$ phase step is 2.09V. Figure 4.2 shows that the linearity of this phase shifter is good as well. Figures 4.3, 4.4 and 4.5 indicate that the tilt and non-uniformity of this specific PZT phase shifter is very small.

From the obtained results of hundreds of tests, the average driving voltage to get $\pi/2$ phase step is determined at 2.13V for this apparatus. The standard deviation for these tests is 0.104 V, which implies very good stability for this PZT phase shifter setup.
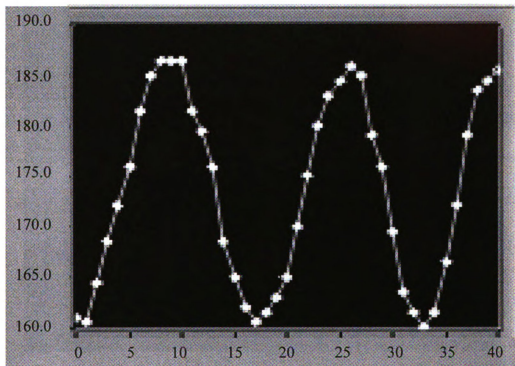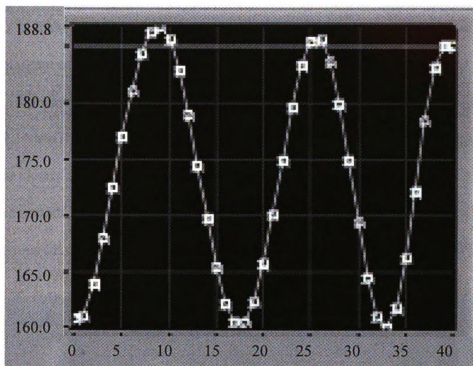
Figure 4.7. Recorded intensity waveform.

Figure 4.8. Fitting curve obtained by IMMS.

A modified phase shifter is presented in Figure 4.9. A large mirror is attached to the PZT by some adhesive putty. The behavior of this PZT mirror was checked by performing the newly developed calibration method. A recorded intensity wave is presented in Figure 4.10. After signal processing, a smooth curve is obtained as seen in Figure 4.11. The proposed calibration method is performed to obtain the phase-driving voltage diagram as shown in Figure 4.12. The linearity is seen to be good in this graph. Figure 4.13 presents the 3-D graph of phase shifting along the two edges of the image. In Figures 4.14 and 4.15, the tilt and non-uniformity of the phase shifting motion can be seen more clearly. This phase shifting setup is not so uniform as the previous one, and tilt is obvious in both X and Y directions. The calibration test was repeated 30 times for this setup. Serious tilt of the mirror is always observed. Linearity is not consistent either.

Figure 4.9.The phase shifter.
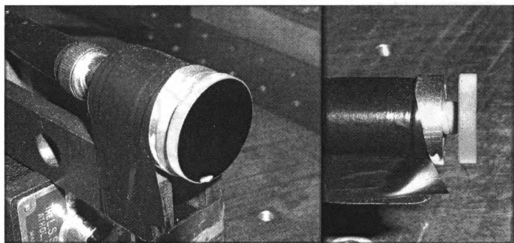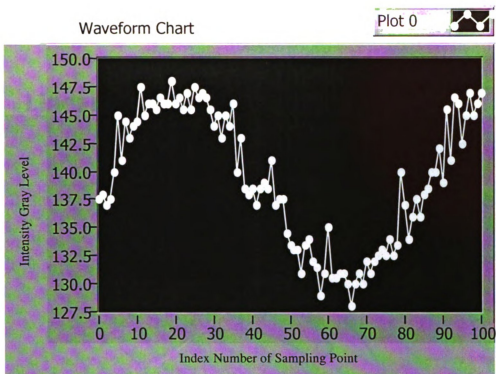
Figure 4.10. Intensity curve at one pixel point obtained by phase shifting.

Figure 4.11. The fitting intensity curve of the Figure 4.11.
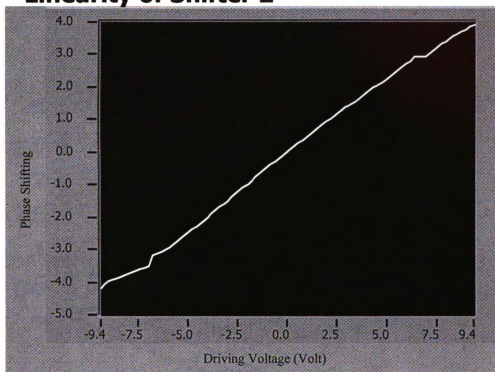
Linearity of Shifter 2

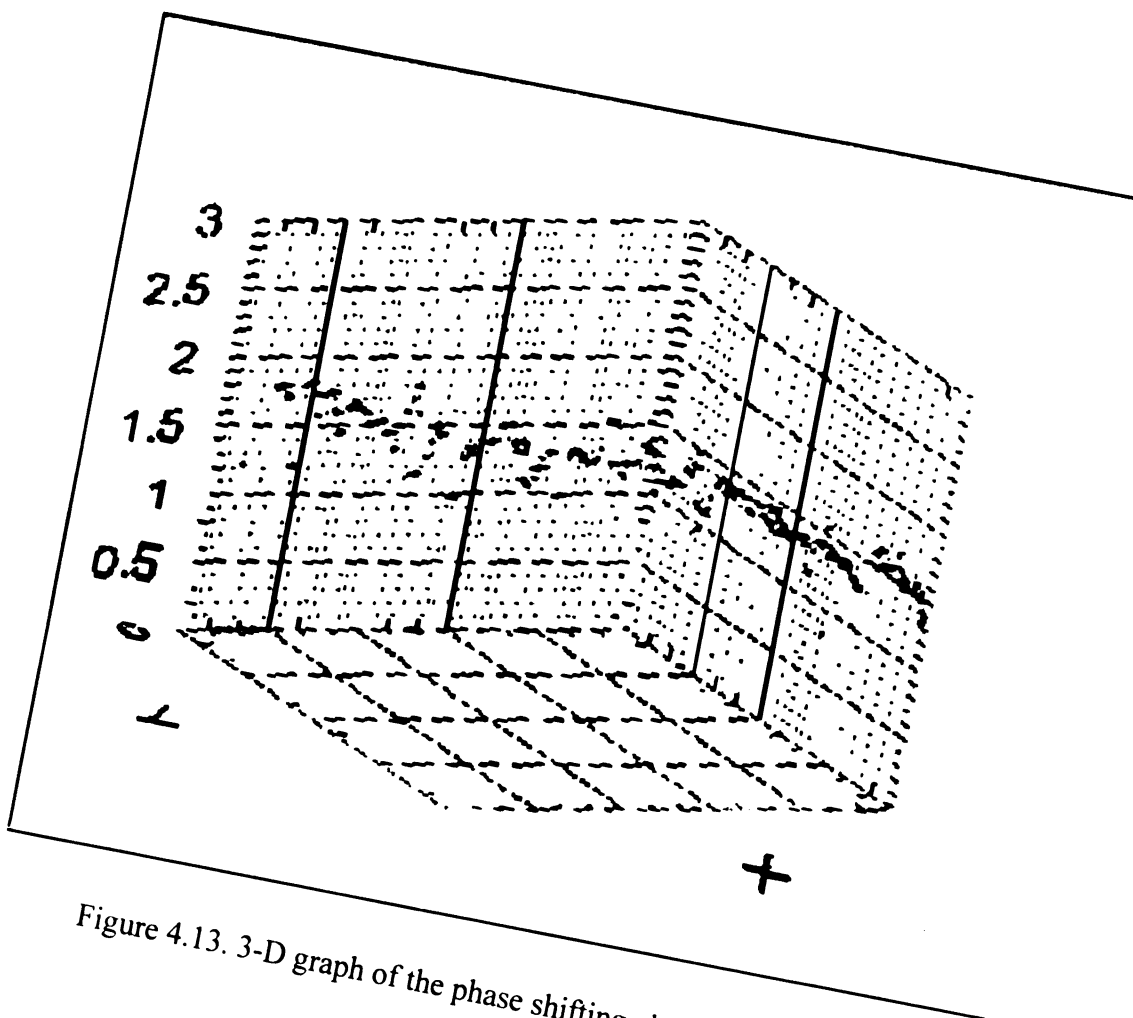Figure 4.12. Phase step versus driving voltages.

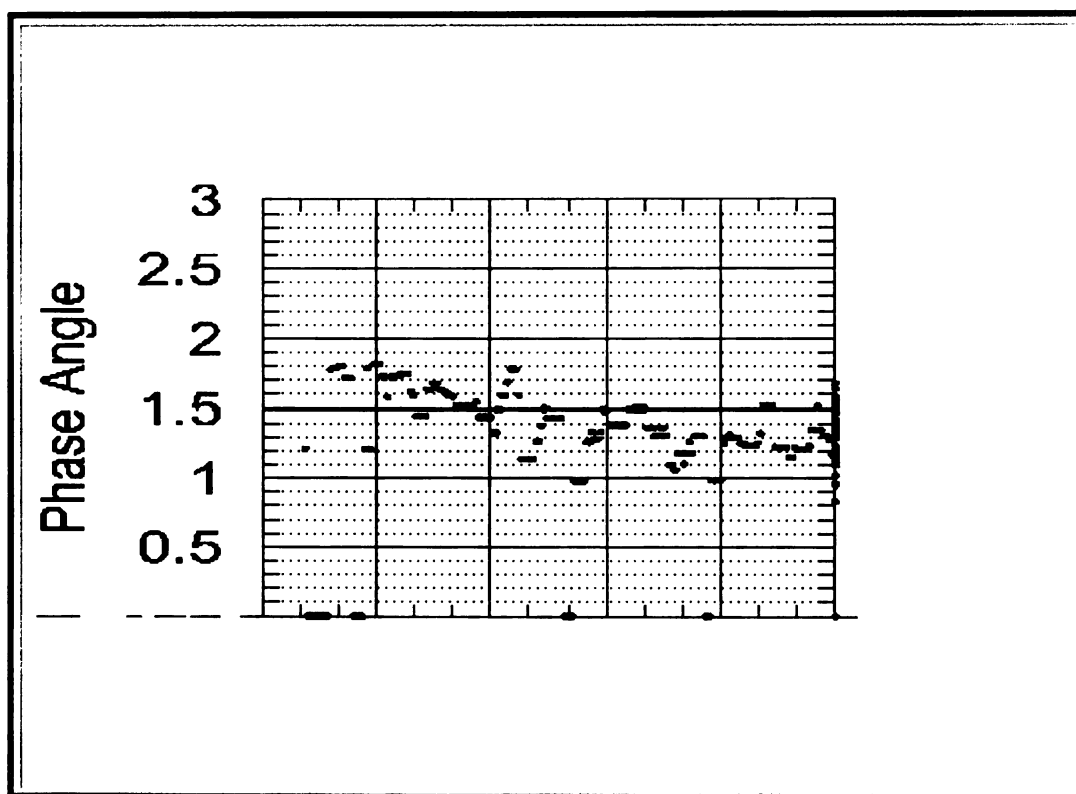Figure 4.13. 3-D graph of the phase shifting along X and Y axis.

Figure 4.14. Tilt and non-uniformity in x-direction.
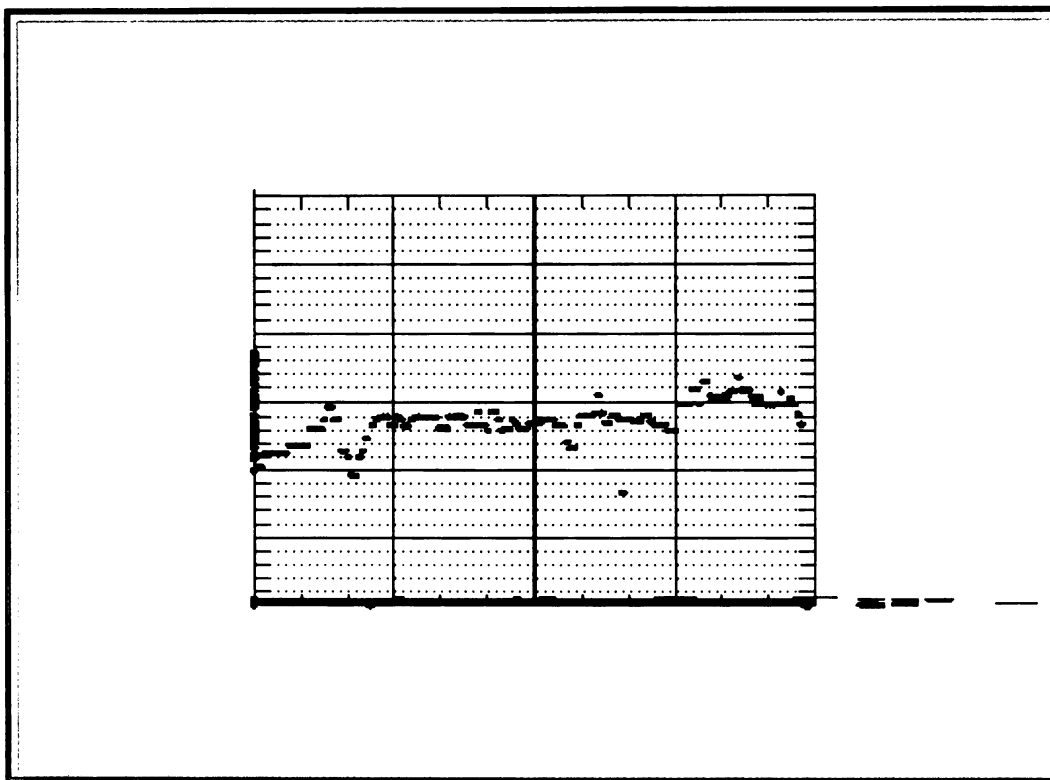
Figure 4.15. Tilt and non-uniformity in y-direction.

4.4 Advantages of the new technique

A new technique to calibrate the phase shifting has been derived from the IMMS method, and its applications to PZT phase shifters were successfully demonstrated in repeated experiments. This algorithm shows several practical advantages. First, it eliminates the drawbacks caused by the common assumption of the linearity and uniformity of the phase shifter, thus efficiently minimizing the movement error of the PZT. Secondly, it can be used to inspect several working parameters of the phase shifter simultaneously, such as non-linearity, non-uniformity and tilt of the phase shifter.

Overall, this new method is a convenient and ideal way to calibrate the phase shifter, to inspect the quality of the phase shifter, and to evaluate the reliability of the experimental setup. Whenever the experimental setup is adjusted, such as the illumination angle or the path length of beam, this algorithm can implement calibration and inspection online very conveniently.

Chapter 5. Simplified DSPI setups

Through use of the IMMS method developed in Chapter 3, the in-plane DSPI setup can be simplified and perform quantitative measurements. As well, a simple out-of-plane setup patented by Cloud (2000) can measure out-of-plane displacement quantitatively by the application of the IMMS method.

5.1 A simple in-plane DSPI set up

5.1.1 Introduction

Since the first demonstration of Electronic Speckle Pattern Interferometry (ESPI) almost simultaneously by Macovski, Ramsey, and Schaefer (1971) in the United States and by Butters and Leendertz (1971) in England, the majority of research work on ESPI techniques has focused on the development of the phase shifting techniques, phase unwrapping algorithms and digital filter applications (e.g. Creath 1985, Fornaro, et al. 1996, Hibino 1999, Kaufmann, 1998, Sesselmann and Goncalves 1998, Surrel 2000). The goals of these investigations have largely been to obtain more accurate numerical results or to simplify the digital signal processing. Relatively little research has been published about modifying the system of apparatus of the ESPI. Siebert, Wegner and Ettemeyer (2001) introduced a compact ESPI sensor that can be attached to the test object, but the construction of this sensor is still a trade secret. Two basic well-known practical in-plane sensitive ESPI setups were introduced by Jones and Wykes (1983) as seen in Figure 5.1. Most research work to date has been done using the illumination arrangement

86

of Figure 5.1 (a) or variations thereof. The setup of Figure 5.1 (b) is similar to that used by Post, Han, and Ifju (1994) to generate virtual gratings for moiré interferometry.

As far as the author can discern, no quantitative DSPI measurement results based on the second arrangement shown in Figure 5.1. (b) have been reported. The most plausible reason is that it is very difficult to employ phase shifting techniques to obtain quantitative results because: (1) it is hard to make a big PZT mirror that is stiff, stable, and of reasonable mass, (2) driving a large reflection mirror to do phase shifting is much more difficult than driving a very small mirror such as is commonly used in the first setup. The tilt, twist, and deformation of the large mirror are difficult to handle with conventional phase shifting and data reduction processes. However, the advantages of this setup are very attractive for practical applications of DSPI. This arrangement forms a nearly-common-path interferometer, which implies excellent noise immunity and fewer components used than are needed in the first arrangement. The Improved Max-Min Scanning phase shifting algorithm has a good immunity to tilt, non-linearity and non-uniformity of phase shifting and vibration noise as reported in Chapter 3. Consequently, this IMMS method can be a good choice to make the Figure 5.1 (b) setup work quantitatively. The next section demonstrates that, with the IMMS method, the in-plane ESPI setup can be simplified very much and the noise tolerance of DSPI can be improved significantly.

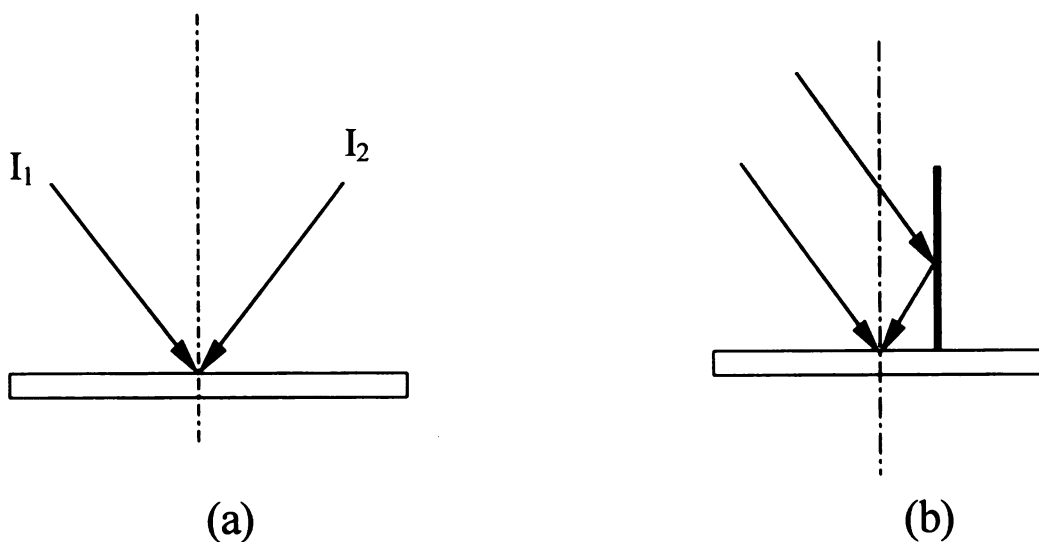Figure 5.1. Two basic practical illumination apparatus of in-plane speckle interferometry.

5.1.2 Setup and Tests

Figure 5.2 is a diagram of the in-plane ESPI setup developed in this work. A plane
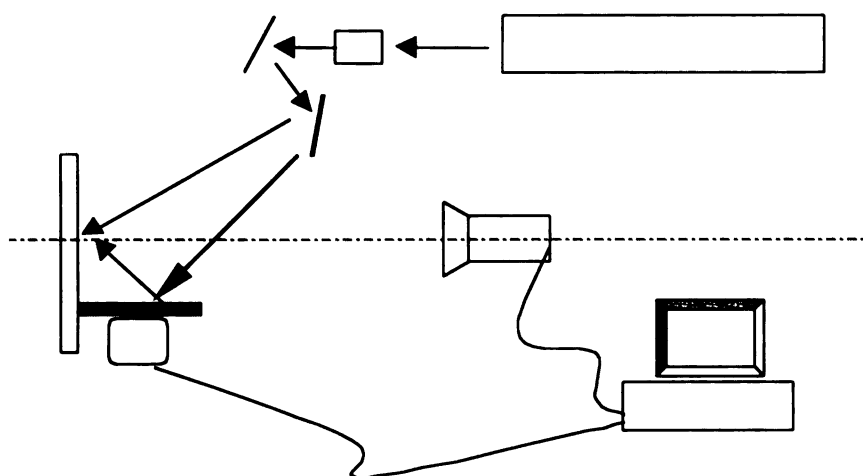
Figure 5.2. The arrangement used in this work.

mirror is placed in front of the object and is perpendicular to the object surface. This mirror reflects half of the illumination beam to provide a second in-plane illuminating beam while the other half illuminates directly in a symmetrical direction. The nearly common path of the two illuminating beams gives this setup a better environmental tolerance. Furthermore, the reflection mirror could be attached to the object. This should further improve the noise immunity of the setup. Figure 5.3 is a photo of the entire simple setup. The reflection mirror is attached to a small PZT by adhesive putty (right part of the Figure 5.3).
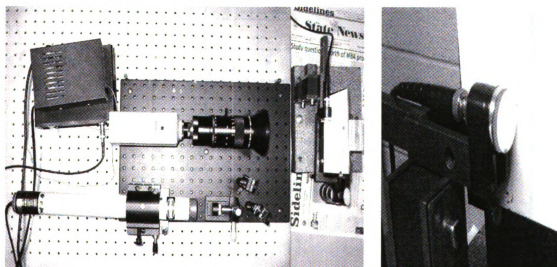
Figure 5.3. The experimental setup and the PZT mirror.

To check the behavior of the PZT-reflection mirror, the phase shifter calibration technique proposed in Chapter 4 was used to calibrate the behavior of the PZT-drive mirror. In Figure 5.4 and 5.5, the tilt and variance of the spots indicate that the tilt and non-uniformity of this PZT-mirror are very significant over the entire image area. It is impossible to obtain reliable phase measurement by using the common phase shifting techniques such as four-step phase shifting.

Figure 5.4. The tilt and non-linearity of the PZT mirror in the horizontal direction.
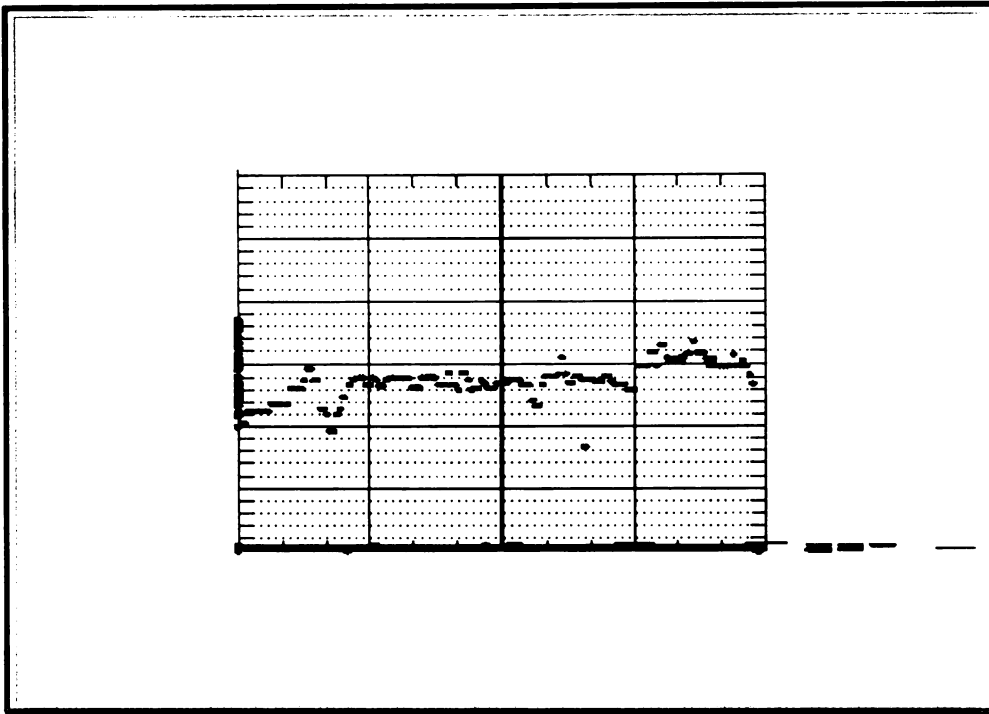
Figure 5.5. The tilt and non-linearity of the PZT mirror in the vertical direction.

To compare the immunity to noise of the setup, both in-plane DSPI arrangements

shown in Figure 5.1 were used to construct correlation fringe maps. In this test, the

specimen was placed on a normal table as seen in Figure 5.3 instead of the vibration–
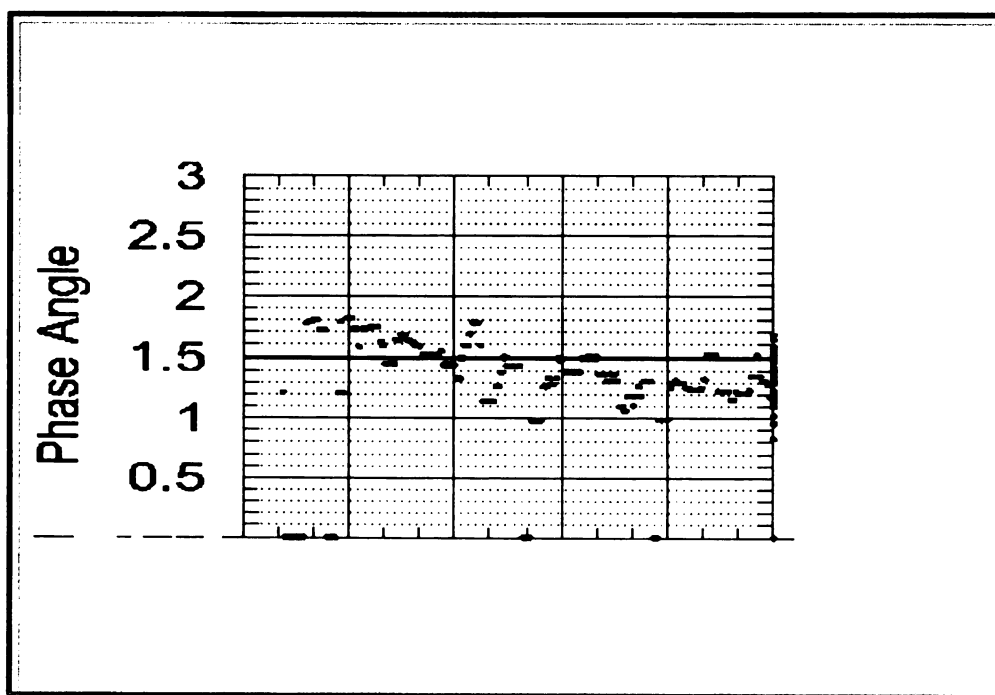
insulated table. Consequently, the vibration of floor will severely affect the measurement

results. Figure 5.6 presents the comparison of the correlation fringe patterns obtained by

both arrangements simultaneously. In the fringe graph, the left part of the vertical curve

in this picture was obtained by the Figure 5.1 (b) arrangement. The right part of it was

obtained by Figure 5.1 (a) arrangement. The comparison in this figure indicates that it is

impossible for the Figure 5.1 (a) setup to provide a stable correlation fringe map, which

indicates it cannot perform measurements under such a noisy condition. The Figure 5.1

(b) arrangement produces more stable fringe maps and presents an excellent immunity to noisy environments.
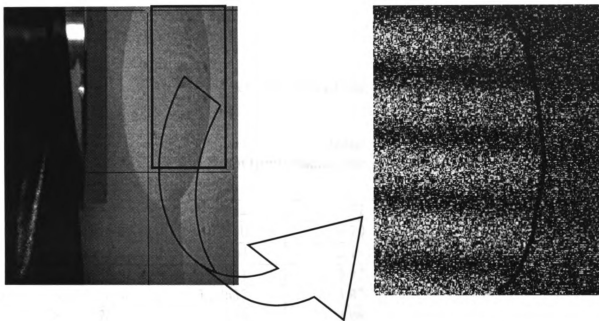
Figure 5.6. The comparison between two arrangements of DSPI.

To make the simple in-plane setup work quantitatively, the phase shifting method must be robust to tilt, non-uniformity and non-linearity. The previous work about the IMMS phase shifting method demonstrated that the IMMS method meets the above demands. Therefore, the IMMS phase shifting method was employed to process the acquired signals. In-plane displacement measurements were performed to test this apparatus. The displacement calibration plate was placed on a normal table, which is very vulnerable to vibrations.

Known displacement induced by a micrometer was measured by the setup in Figure 5.3 with IMMS technique. Table 5.1 shows the comparison between the DSPI measurements and induced displacements. Even under such a noisy condition, good agreement is observed.

Table 5.1. The comparison between induced and measured results.

Rotation angle (Rad)	Induced displacement (μm)	Measured displacement (μm)	Difference (%)
2.15254e-4	0.98552	1.01	-2.48397
3.44407e-4	1.62560	1.70	-4.57677
4.30508e-4	2.07264	2.19	-5.66234
6.45763e-4	3.07848	3.12	-1.34872
8.61017e-4	3.57632	3.47	2.972888
8.61017e-4	4.14528	4.08	1.574803
6.45763e-4	5.18160	5.18	0.030878
8.61017e-4	2.43840	2.60	-6.6273
4.30508e-4	2.56032	2.74	-7.01787

5.2 A simple out-of-plane DSPI setup

Several variants of a simple out-of-plane sensitive DSPI setup were reported and patented by Cloud (2000, 2003). Figure 5.7 is a schematic of one of these arrangements. In this setup, a glass scattering plate is placed in front of the specimen. When the laser beam passes through the scattering plate to illuminate the specimen, part of the illuminating beam is reflected directly into the imaging system to provide the reference beam. The camera has a very narrow viewing angle with the illumination beam, allowing this arrangement to be sensitive to out-of-plane displacement. The nearly common path character of this arrangement gives this setup an excellent noise tolerance, which was observed while obtaining correlation fringe maps without an optics table. As mentioned by Cloud (2000), to make this simple setup able to measure out-of-plane displacement quantitatively, an appropriate method for phase map determination is desired. A driver to move or tilt the ground-glass plate seems the simplest way to perform phase shifting technique in this apparatus. However, the mass and limited stiffness of the plate will result in severe unwanted errors for phase evaluation, such as vibration and uneven movement throughout the entire plate, when conventional processing is used. Considering the characteristics of the new IMMS method developed in this work, it can be a good alternative algorithm to perform phase evaluations for this set up.
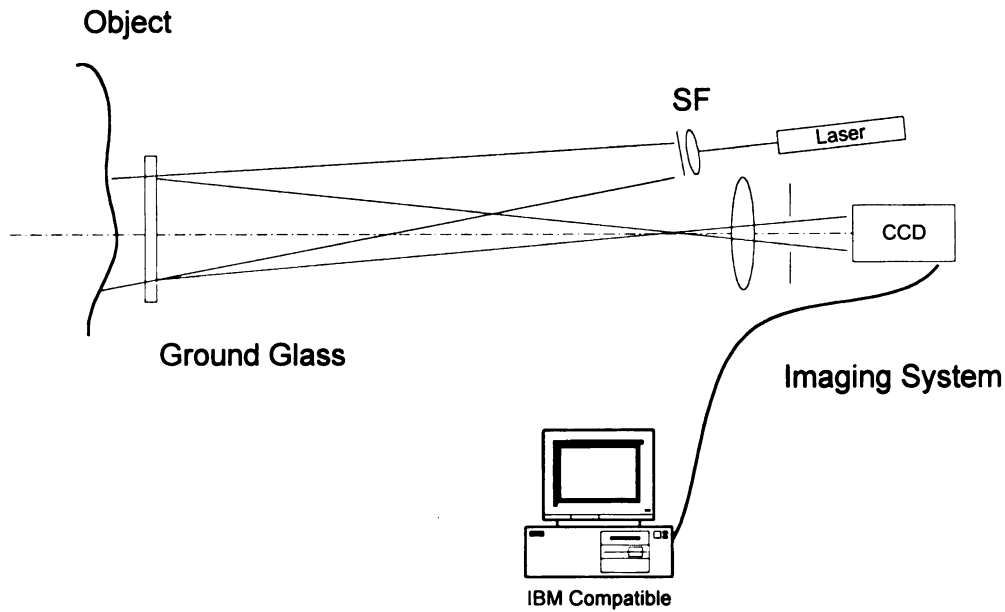
Figure 5.7. Schematic of the simple out-of-plane sensitive DSPI system.

Figure 5.8 shows such an out-of-plane DSPI device. In this apparatus, a PZT is attached to the plate by adhesive putty to drive the plate to perform phase shifting. Figure 5.9 is the picture of the PZT plate. The plate is flexibly suspended at three points, two at the bottom edge, and one close to the middle point of the upper edge. The driving point is nearly the center of the plate. It is obvious that the driving motion involves both deformation and tilt of the glass plate, so it is definitely not uniform throughout the area of interest.
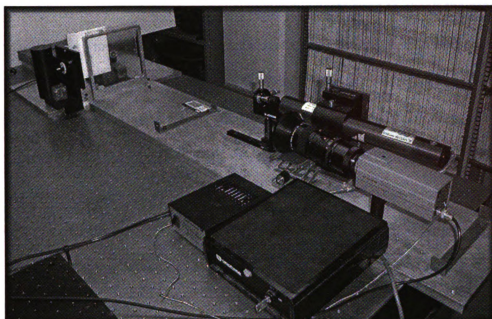
Figure 5.8. The Out-of-plane DSPI setup.
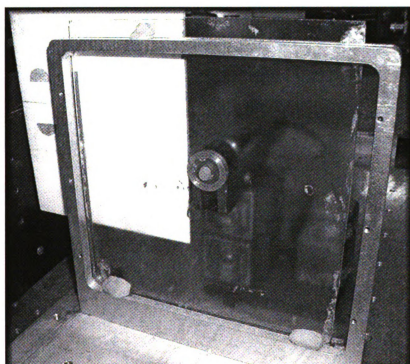
Figure 5.9. The phase shifting plate.

The calibration method developed in Chapter 4 is performed to check the properties of the phase shifting motion. Figure 5.10 is the initial speckle image. The PZT transducer shows in the right part in this image. Figure 5.11 shows that the linearity is not bad at this pixel point of the image. Figure 5.12 is a 3-D graph of the phase shifting along two edges of the region of interest. Figure 5.13 indicates that the tilt is severe along the X direction. Figure 5.14 indicates that the tilt along Y direction is less than that in the X direction, but still severe. Serious non-uniformity of the phase shifting can be seen in both graphs. It is known that the IMMS method can minimize the effect of the tilt and non-uniformity of the phase shifting movement.

Figure 5.10. A speckle picture with the PZT driving setup on the right.

Linearity of Shifter 2
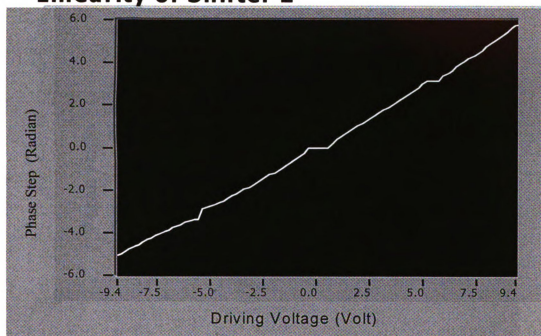
Figure 5.11. The linearity of the phase shifting.
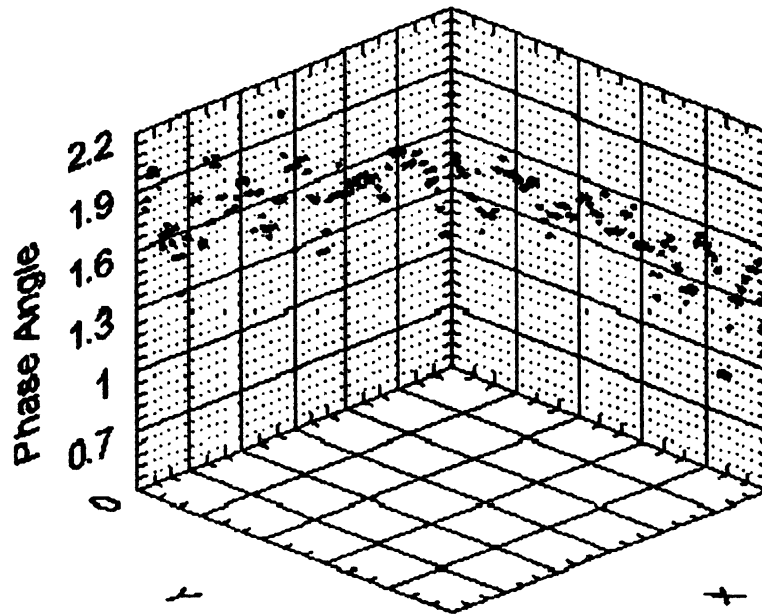
Figure 5.12. The 3-D graph of phase shift.

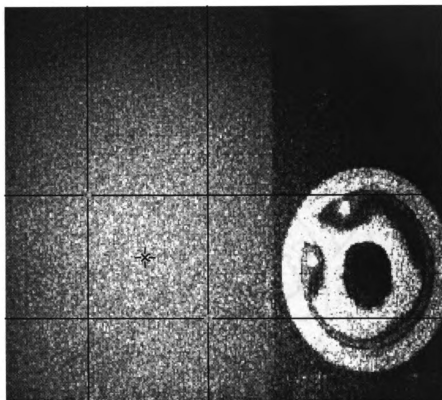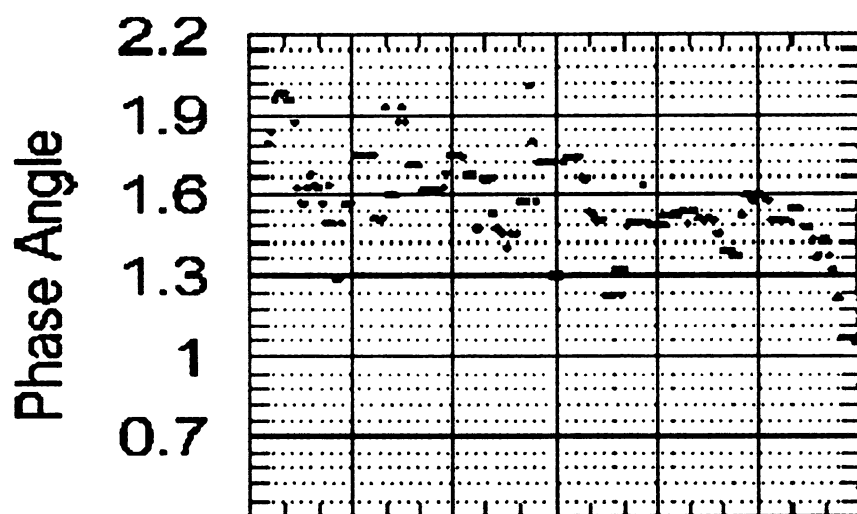Figure 5.13. The tilt and non-uniformity of the phase shifting along the x-direction.
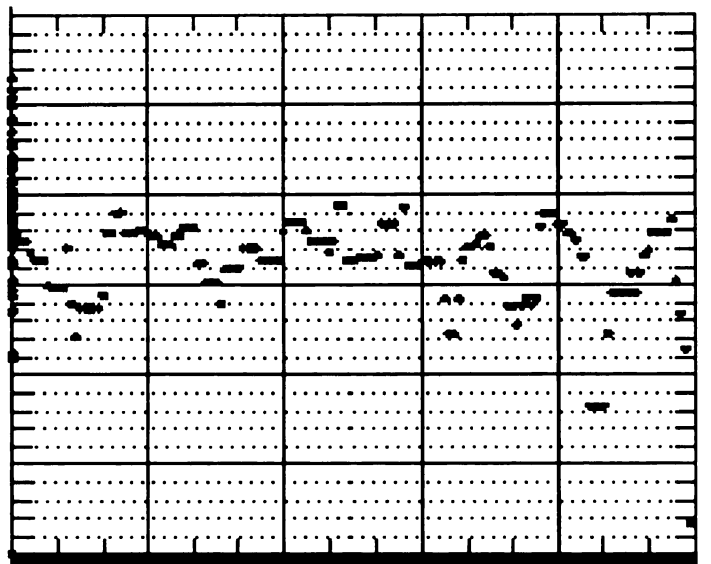
Figure 5.14. The tilt and non-uniformity of the phase shifting along the y-direction.

The IMMS method is applied with this out-of-plane setup to perform signal processing to measure some induced out-of-plane displacement on a calibration plate. Figure 5.15 is a phase change map obtained by IMMS method from an out-of-plane rigid body rotation. Figure 5.16 is the fringe map after filtering of Figure 5.15. Figure 5.17 is the measured distribution of the displacement field. A 3-D graph of the out-of-plane displacement field is presented in Figure 5.17. The measurement tests were repeated, Table 5.2 gives the comparison of the DSPI results and induced displacements. The good agreement between them indicates that this simple out-of-plane DSPI setup works well to measure out-of-plane displacement quantitatively.
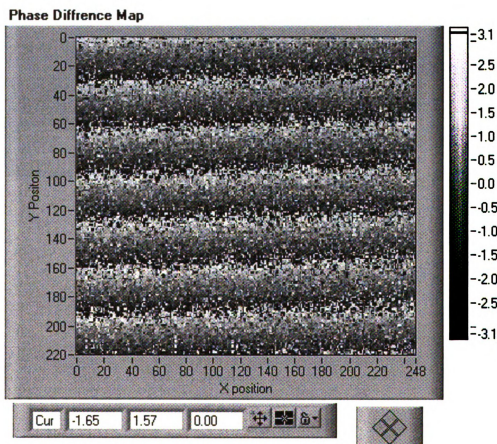
Figure 5.15. A raw phase difference map.
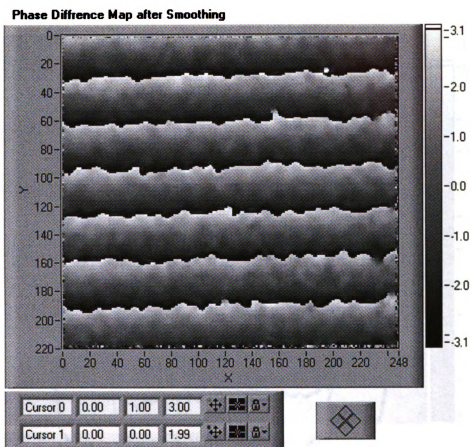
Figure 5.16. The phase difference map after filtering.

Displacement Field
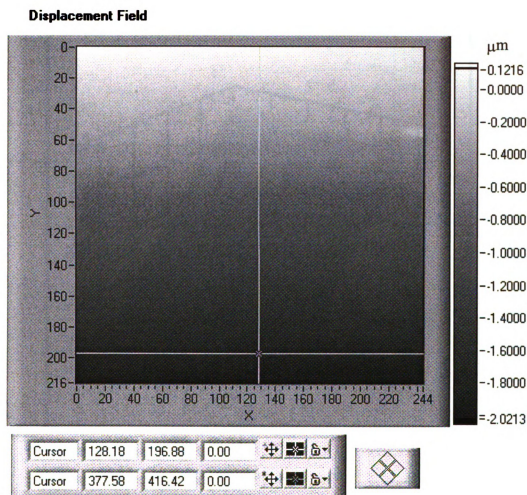
Figure 5.17. The measured displacement field in gray scale.
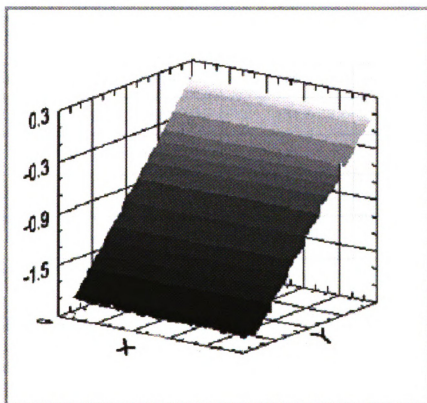
Figure 5.18. The 3-D map of out-of-plane rigid body rotation.

Table 5.2. The comparison between induced and measured results

Rotation angle (Rad)	Induced Displacement (μm)	Measured displacement (μm)	Difference (%)
4.84322e-5	1.0129	1.06	-4.648
7.5339e-5	1.5372	1.54	-0.18076
7.5339e-5	0.7686	0.73	5.0234
8.61017e-5	1.9764	1.91	3.36098
8.61017e-5	2.0203	1.96	2.9870

5.3 Conclusions

In this chapter, both the in-plane DSPI and out-of-plane DSPI were simplified very much compared to the commonly used setups. This makes the DSPI setup more cost effective. These simplified setups were shown to work quantitatively with the IMMS phase shifting method. Very good noise immunity of the presented setups was seen. This broadens the application of the DSPI technique to some noisy service environments outside the laboratory.

Chapter 6. Summary and discussions

In this study, an IMMS method was developed for phase evaluation. The IMMS method demonstrated a good immunity to some particular noise. As well, a new technique based on the IMMS was developed to calibrate the behavior of PZT phase shifters in real-time. By applying the IMMS technique, both in-plane and out-of-plane DSPI setups were simplified.

An improved Max-Min scanning method for phase determination has been presented in Chapter 3, and its application to the determination of phase maps was successfully demonstrated in some DSPI experiments to measure crack length on a CT specimen and surface displacement fields on a calibration plate.

The new IMMS algorithm has several practical advantages over the other traditional methods. The least-square curve-fitting method and the digital filters applied in this technique allow the maximum and minimum intensity values to be estimated more accurately than with other techniques. This improvement is achieved because the intensity waveform can be fitted well from recorded signals through more cycles of the intensity waveform. Under ideal test conditions, such as on a vibration-insulated table in a laboratory and an excellent linear phase shifter, this new algorithm does not have advantages over other phase shifting techniques. However, in some noisy situations, since signal-processing techniques in the time domain can be employed to the recorded intensity signals, the improved algorithm is proved to have a better environment tolerance. For instance, the low pass filter used in this work could remove vibration

noise efficiently. Furthermore, the sign of the phase angle can be determined by the gradient of the fitting curve directly, so the requirement for additional images to determine signs becomes unnecessary, meaning the elimination of the difficult steps to manipulate the phase shifter carefully to obtain some tiny phase shifting steps as mentioned by Vikhagen (1990).

With the IMMS method, the requirement to calibrate the phase shifter is removed completely, because the phase steps are arbitrary and need not even be known. Since only the intensity changes are used to determine maximum and minimum intensity and the phase shifting step length is less important, the non-linearity of the phase shifter does not significantly affect the accuracy of results. Based on point-by-point analysis of the intensity wave, non-uniform phase shifting over the whole image does not significantly affect the result. Compared to the common assumption for most traditional methods that the phase shifting has a good linearity, these features of the IMMS minimize the requirements for the phase shifter very much and enhance the noise tolerance of the phase evaluations.

Even more significantly, with slow deformation, such as deformation under thermal loading or digitally controlled loading, ideal intensity signals can be recorded during the object deformation, so that the phase shifter could be entirely removed from the experimental setup. The same is true if there are path length changes caused by, say, thermal drift in optic elements. So, the method uses to advantage what have been sources of error or problems in conventional approaches.

It has to be clearly pointed out that the intensity waveform at each pixel plays a key role in this algorithm. The curve fitting technique is an ideal method to obtain a good

intensity waveform. A sinusoid least square fitting method was published many years ago by Ransom, et al. (1986) and Macy, et al. (1983). In the sinusoid fitting method, the fitting model is fixed to $I(v)=a(v)+b(v)Cos(\varphi(v))$. After solving a series of equations, parameters, $a(v)$, $b(v)$ and $\varphi(v)$ are determined. In the improved method presented in this work, the fitting parameters are not the goal of the performance of the fitting techniques. As mentioned in chapter 3, only the intensity-changing curve is desired from fitting techniques. Therefore, the fitting model is very flexible. Furthermore, there are more options of commercial curve fitting software that are appropriate to the task. More significantly, some options have better tolerance of non-linearity of the PZT compared to the sinusoid fitting method.

In Chapter 3, the noise tolerance of the developed IMMS method is discussed. Noise signals obtained from different situations were added to some sample recorded signals and the developed IMMS method was employed to process these noisy data. It is shown that the IMMS method has a good tolerance to some specific noise signals, particularly to high frequency noise and to small amplitude low frequency noise. This brings an advance to DSPI technology's application in factory environments.

A disadvantage of this method is that, to construct the intensity waveform, many image frames need to be recorded, which means that large numbers of image signals have to be dealt with. Current high-speed computers make the improved algorithm practicable to determine phase values in a short time.

Based on the developed IMMS method, a new technique to calibrate the phase shifting behavior has been derived in Chapter 4, and its applications to check the behavior of a PZT phase shifter was successfully demonstrated in some experiments.

This technique uses the IMMS method to compute the phase values along the entire intensity waveform to obtain the diagram of phase shifting versus the driving voltages to the PZT at some pixels so that the linearity of the phase shifting can be clearly displayed on the diagram. By considering more pixel points along various directions over the image, the tilt and non-uniformity of the phase shifting can be shown in a 3-D graph. This calibration algorithm shows several practical advantages. First, it eliminates the drawbacks caused by the common assumption of the linearity and uniformity of the phase shifter, thus efficiently minimizing the movement error of the PZT. Secondly, it can be used to inspect a few properties of the phase shifter simultaneously, such as non-linearity, non-uniformity and tilt of the phase shifter.

Overall, this new method is a very convenient way to calibrate the phase shifter, to inspect the quality of the phase shifter, and to assess the reliability of the experimental setup. Whenever the experimental setup is adjusted, such as the illumination angle or the path length of beam, this algorithm can implement calibration and inspection in real-time very conveniently.

Since the IMMS method shows good environment tolerance, particularly minimizing the effect of errors of phase shifting, both the in-plane DSPI and out-of-plane DSPI were simplified very much compared to the commonly used setups. In Chapter 5, these simplified setups were shown to work quantitatively with the IMMS phase shifting method. Very good noise immunity of the presented setup was seen. This simplification makes the DSPI setup more cost effective and broadens the application of the ESPI technique to noisy service environment outside the laboratory.

Chapter 7. Conclusions and recommendations

- A new algorithm for phase determination that uses digital filters and curve fitting techniques, called the IMMS method, was developed and verified.

- The IMMS technique was successfully used to measure crack length on compact tension (CT) specimen.

- The IMMS technique shows good noise tolerance.

- The IMMS technique doesn't require phase shifting calibration as needed for other techniques.

- The IMMS technique can be used to perform on-line calibration of the behavior of PZT phase shifter including driving voltage calibration, effect of tilt, non-uniformity, and no-linearity.

- In some circumstances, for instance, under conditions of thermal loading or digitally controlled loading, the IMMS technique allows elimination of phase shifters.

- By employing the IMMS method, simple DSPI setups were developed and applied to perform out-of-plane and in-plane displacement/deformation measurements.

- The simple DSPI setups show good noise tolerance.

Recommendations for future work:

1. Based upon the simplified DSPI apparatus, it is possible to develop some compact DSPI sensors to measure displacement and deformation. The sensors will be very portable and even can be attached to objects.

2. A processing program can be developed to use a series of continuously recorded images to measure large displacements, which can eliminate the limitation of decorrelation and memory loss.

3. Apply the simplified DSPI setup to measure slow deformation, such as the deformation under thermal loading or digitally controlled loading, so that the phase shifter can be removed from the DSPI setup completely.

REFERENCES

Brug, H. V. (1999). "Phase-step calibration for phase-stepped interferometry," App. Opt., 38(16), 3549-3555.

Chen, M. Y, Guo, H. W. and Wei, C. L. (2000). "Algorithm immune to tilt phase-shifting error for phase-shifting interferometers," App. Opt., 39(22), 3894-3898.

Chen, X., Gramaglia, M. and Yeazell, J. A. (2000). "Phase-shifting interferometry with uncalibrated phase shifts," App. Opt., 39(4), 585-591, 2000.

Cheng, Y. Y. and Wyant, J. C. (1985). "Phase shifter calibration in phase-shifting Interferometry," App. Opt., 24(18), 3049-3052.

Cloud, G. L. (1979). "Practical speckle interferometry for measuring in-plane deformations," App. Opt., Vol. 14, No. 4, pp. 878-884.

Cloud, G. L. (1995). *Optical Methods of Engineering Analysis*, Cambridge University Press, New York

Cloud, G. L. (2000). United States Patent 6128082.

Cloud, G. L. (2003). "Speckle interferometery made simple and cheap," Experimental Techniques, 27(4), 27-30.

Cloud, G. L., Ding, X. and Raju, B. B. (2002). "Real-time digital speckle interferometry to measure crack length," Experimental Techniques, 26(1), 19-21.

Creath, K. (1985). "Phase-shifting speckle interferometry," App. Opt., 24(18), 3053-3058.

De Groot, P. (1995). "Derivation of algorithms for phase-shifting interferometry using the concept of a data-sampling window," App. Opt., 34(22), 4723-4730.

Ding, X. (2002). "Improved signal processing for max-min scanning method for phase determination," Student Paper, 2002 SEM Conference on Experimental and Applied mechanics, Milwaukee, WI.

Ding, X. Cloud, G. L., Raju, B. B. (2004a). "Noise tolerance of improved max-min scanning method for phase determination," Proceedings of 2004 SEM X International Congress & Exposition, Society for Experimental Mechanics.

Ding, X., Cloud, G. L., Raju, B. B. (2004b). "Improved signal processing algorithm for the max-min scanning method for phase determination," Optical Engineering, Vol. 43, No. 1, pp. 63-68.

Farrell C. T. and Player, A.M. (1992). "Phase step measurment and variable step algorithms in phase shifting Interferometry," Measurement science and technology, 2(10), 953-958.

Farrell, C. T. and Player, A. M. (1994). "Phase-step insensitive algorithms for phase-shifting interferometry," Measurement science and technology, 5 (6), 648-652.

Fornaro, Gianfranco, Franceschetti, Giorgio, and Lanari, Riccardo, (1996). "Robust phase-unwrapping techniques: a Comparison," J. Opt. Soc. Am. A, 13(12), 2355-2366.

Gens, R. (2003). "Two-dimensional phase unwrapping for radar interferometry: developments and new challenges," International Journal of Remote Sensing, 24(4), 703-710.

Ghiglia, D. C. and Romero, L. A. (1996). "Minimum L^P-norm two-dimensional phase unwrapping," J. Opt. Soc. Am., 13, 1999-2012.

Goldberg, K. A. and Bokor, J (2001). "Fourier-transform method of phase-shift determination," App. Opt., 40(17), 2886-2894.

Greivenkamp, J. E. (1984) "Generalized data reduction for heterodyne interferometry," Opt. Eng. 23(4), 350-352.

He, X. Y., Kang, X., Tay, C. J., Quan, C. G., ang Shang, H. M. (2002). "Proposed algorithm for phase unwrapping," App. Opt., 41(35), 7422-7428.

Herráez, M. A., Gdeisat, M. A. Burton, D. R., and Lalor M. J. (2002). "Robust, fast, and effective two-dimensional automatic phase unwrapping algorithm base on image decomposition," App. Opt., 41(35), 7445-7455.

Hibino, K. (1999). "Error-compensating phase measuring algorithms in a Fizeau interferometer," Optical Review, 6(6), 529-538.

Hibino, K., Oreb, B. F., Farrant, D. I., and Larkin, K. G. (1995). "Phase shifting for nonsinusoidal waveforms with phase-shift errors," J. Opt. Soc. Am. A, 12(4), 761-768.

Hong, S. S. (1997). "*Digital image processing algorithms for electronic speckle pattern interferometry,*" Master thesis, Michigan state University.

Huang, M. J. and Lai, C. J. (2002). "Innovative phase unwrapping algorithm: hybrid approach," Optical Engineering, 41(6), 1373-1386.

Jones, R. and Wykes, C. (1983). *Holographic and Speckle Interferometry.* Cambridge University Press.

Kaufmann, G. H., Ruiz, P. D. and Galizzi, G. E., (Jul. 1998). "Unwrapping of digital speckle pattern interferometry phase maps using a minimum L-norm algorithm," Proc. SPIE, 3478, 170-180.

Koliopoulos, Chris L. (1996). "Phase shifting techniques applied to unique applications," Proc. SPIE 2861, 86-93.

Larkin, G. and Oreb, b. F. (1992). "Design and assessment of symmetrical phase shifting algorithm," J. Opt. Soc. Am. A, 9(10), 1740-1748.

Macy, W. W., Jr., and Bokor, J. (1983) "Two-dimensional fringe-pattern analysis" App. Opt., 22(23), 3898-3901.

Melozzi, M., Pezzati, L. and Mazzoni, A. (1995). "Vibration insensitive inerferometer for on-line measurements," App. Opt., 34(25), 5595-5601.

Okada, K., Dato, A. and Tsujiuchi, J. (1991). "Simultaneous calculation of phase distribution and scanning phase shift in phase shifting inerferometry," Optics Communications, 84(3, 4), 118-124.

Phillion, D. W. (1997). "General methods for generating phase shifting interferometry algorithms," App. Opt., 36(31), 8098-8115.

Post, D., Han, B. and Ifju, P. G. (1994). *High Sensitivity Moiré: Experimental Analysis for Mechanics and Materials.* New York: Springer-Verlag.

Ransom, P. L. and Kokal, J. V. (1986) "Interferogram analysis by a modified sinusoid fitting technique," App. Opt., 25(22), 4199-4204.

Ruiz, P. D., Huntley, J. M., Shen, Y. J., Coggrave, C. R., Kaufmann, G. H., (2001). "Vibration-induced phase errors in high-speed phase-shifting speckle-pattern interferometry, " App. Opt., 40(13), 2117-2125.

Sesselmann, M., Goncalves, A. A. Jr., (Jul. 1998). "Single phase step algorithm for phase difference measurement using ESPI," Proc. SPIE 3478, 153-159.

Strand, J. and Taxt, T. (1999). "Performance evaluation of two-dimensional phase unwrapping algorithms," App. Opt., 38(20), 4333-4344.

Surrel, Y. (1996). "Design of algorithms for phase measurements by the use of phase stepping," App. Opt., 35(1), 51-60.

Surrel, Y., (2000). "Fringe analysis," Topics in Applied Physics, 77, 55-102.

Siebert, Th., Wegner, R.and Ettemeyer, A. (2001). "Combine simulation and experiment in automotive testing with ESPI measurement," Proceeding of SEM, 2001 SEM Conference on Experimental and Applied mechanics, Portland, Oregon.

Vikhagen, E. (1990). "Nondestructive testing by use of TV holography and deformation phase gradient calculation," App. Opt., 29(1), 137-144.

Vrooman, H. A. and Maas, A. M. (1991). "Image processing algorithms for the analysis of phase shifted speckle interference patterns," App. Opt., Vol. 30, No. 13, pp. 1636-1641.

Wang, J., Grant, L. (1995). "Electronic speckle interferometry phase mapping and nondestructive testing techniques applied to real-time, thermal loading," App. Opt., 34(3), 3620-3627.

Zhang, H., Lalor, M. J. and Burton, D. R. (1998). "A new error compensating seven sample phase shifting algorithm and application in 3-D fringe projection profilometry," Proc. SPIE, 3478, 121-132.